Received: 16 November 2021 | Revised: 31 May 2022 | Accepted: 2 June 2022

DOI: 10.1111/jmg.12687

Journal of METAMORPHIC GEOLOGY WILEY

ORIGINAL ARTICLE

HTLP metamorphism and fluid-fluxed melting during multistage anatexis of continental crust (N Sardinia, Italy)

Leonardo Casini[1] | **Matteo Maino**[2,3] | **Antonio Langone**[3] | **Giacomo Oggiano**[1] | **Stefania Corvò**[2,3] | **Joan Reche Estrada**[4] | **Montserrat Liesa**[5]

[1]Department of Chemistry, Physics, Mathematics and Natural Sciences, Università di Sassari, Sassari, Italy

[2]Department of Earth and Environmental Sciences, Università di Pavia, Pavia, Italy

[3]National Research Council, Institute of Geosciences and Earth Resources of Pavia, Pavia, Italy

[4]Departament de Geologia Petrologia i Geoquimica, Universitat Autònoma de Barcelona, Barcelona, Spain

[5]Departament de Mineralogia, Petrologia i Geologia Aplicada, Universitat de Barcelona, Barcelona, Spain

Correspondence
Leonardo Casini, Department of Chemistry, Physics, Mathematics and Natural Sciences, Università di Sassari, Via Piandanna no 4, 07100. Sassari, Italy.
Email: casini@uniss.it

Handling Editor: Prof. Johann Diener

Funding information
Ministerio de Economia, Industria y Competitividad

Abstract

The Variscan high-grade metamorphic basement of northern Sardinia and southern Corsica record lower Carboniferous anatexis related to post-collisional decompression of the orogen. Migmatites exposed in the Punta Bianca locality (Italy) consist of quartz + biotite + plagioclase + K-feldspar orthogneisses, garnet and cordierite-bearing diatexite and metatexites, derived from metasediments. Field evidence, petrographic observations, ELA-ICP-MS zircon and monazite dating and pseudosection modelling suggest that anatexis was apparently episodic involving two main stages of partial melting. Using pseudosection modelling, we infer that the first stage of partial melting is in the upper amphibolite facies (~0.45 GPa at ~740°C). Cordierite overgrowths replacing sillimanite, combined with the composition of plagioclase and K-feldspar, suggest decompression followed cooling below the solidus at low pressures of ~0.3 GPa. The age of the first anatectic event is not precisely constrained because of extensive resetting of the isotopic systems during the second melting stage, yet few zircons preserve a lower Carboniferous age which is consistent with the regional dataset. This lower Carboniferous migmatitic fabric is offset by a network of pseudotachylyte-bearing faults suggestive of cooling to greenschist facies conditions. Garnet/cordierite-bearing diatexites incorporate fragments of pseudotachylite-bearing orthogneiss and metatexites. Pseudosection modelling indicates nearly isobaric re-heating up to ~750°C, followed by further cooling below the solidus. The inferred *P–T* path is consistent with decompression and cooling of the Variscan crust through post-collisional extension and collapse of the thickened orogenic crust, followed by nearly isobaric re-heating at low pressures (~0.3 GPa) yielding to a second melting stage under *LP-HT* conditions. U/Th-Pb monazite ages for diatexite migmatites indicate an upper bound of 310–316 Ma for the second melting stage, suggesting that the second melting stage is coincident with the regional phase of crustal shearing. The cause of the high geothermal gradient required for re-heating during the second melting stage is unknown but likely requires some heat source that was probably related to dissipation of mechanical work

within crustal-scale shear zones. According to this interpretation, some upper Carboniferous peraluminous granite precursors of the Corsica–Sardinia Batholith could be the outcome rather than the cause of the late-Variscan high-T metamorphism.

KEYWORDS
diatexite, monazite dating, pseudosection modelling, pseudotachylite, U–Pb zircon dating, Variscan belt

1 | INTRODUCTION

Melting reactions leading to generation of granitic magma typically occur during high-temperature metamorphism, when the rocks are hot enough to exceed their solidus (i.e. Johannes, 1984). Three different types of models might account for the attainment of high temperature in the crust, such as (i) increase of mantle heat flow (Davies & von Blanckenburg, 1995), (ii) enrichment of U, Th, K and other heat-producing elements in the crust (Lexa et al., 2011) and (iii) shear heating (Burg & Gerya, 2005; Nabelek & Liu, 1999). Several high-temperature low-pressure (*HTLP*) metamorphic terrains provide convincing evidence supporting a strong thermal input from the mantle due to either lithospheric extension (Albarède & Michard-Vitrac, 1978; Ducoux et al., 2019; Marotta & Spalla, 2007; Zhang et al., 2018) or syn-collisional slab breakoff (Davies & von Blanckenburg, 1995). As a side effect, both mechanisms trigger extensive melting of the sub-continental mantle leading to vertical flow of magma and magmatic underplating which, in turn, creates a hybrid conductive-advective geotherm further enhancing HT conditions in the middle and upper crust (e.g. Depine et al., 2008). Alternatively, several authors argue that HTLP metamorphism is most effectively caused by protracted crustal reworking leading to selective enrichment in U, Th, K and other heat-producing elements (Sandiford & McLaren, 2002; Gerdes et al., 2000; Rudnick & Gao, 2003; Jaupart & Marechal, 2007; Kumar et al., 2007; Lexa et al., 2011; De Vraies van Leeuwen et al., 2021). The last model has been demonstrated as an effective thermal source yielding to the development of orogen-scale thermal anomalies that can persist over millions of years (Burg & Gerya, 2005; Nabelek et al., 2001). However, neither of these mechanisms support HT conditions and anatexis in the uppermost crust at a pressure < 0.4 GPa. Enhanced mantle heat flow or concentration of radiogenic elements, in fact, would produce an unreasonably hot temperature in the lower crust (e.g. Depine et al., 2008). Similarly, viscous shear heating would be ineffective over geologically relevant time scales between 0.1 and 10 Ma because of the predominance of conductive dissipation at upper crustal depths (e.g. Burg & Gerya, 2005; Nabelek et al., 2010; Platt, 2015). A further complication for deciphering the heat budget is that all these mechanisms are potentially complementary, at least on a local scale; therefore, the geodynamic significance of HTLP metamorphism remains contentious (Chopin et al., 2020; Pownall, 2015; Savko et al., 2015).

In this paper, we investigate the evolution of a composite migmatite complex exposed in the Variscan crust of northern Sardinia (Italy). Migmatites equilibrated at shallow crustal conditions ($P < 0.3$ GPa) recording a complex metamorphic history which involves two distinct episodes of partial melting. The metamorphic evolution of migmatites is characterized using a combination of structural analysis, petrology and geochronology. Pseudosection modelling, LA-ICP-MS U–Pb zircon and monazite dating of different anatectic melts, as well as pseudotachylite-bearing faults and ductile shear zones developed between the two anatectic events, provide quantitative information on the P–T–t path recorded by migmatites. The results are finally discussed in terms of the potential mechanisms triggering multistage anatexis and development of HTLP conditions in the uppermost crust.

2 | GEOLOGICAL SETTING

2.1 | Principal tectonic and metamorphic events

The South Variscan Belt (Iberian Massif, Pyrenées, Maures-Esterel, Corsica–Sardinia and Calabria, Figure 1a) is a collisional orogen that experienced crustal thickening, high-pressure metamorphism and partial melting from Late Devonian to Early Carboniferous times, followed by post-collisional extension and HT metamorphism in the middle-upper Carboniferous and Permian (Matte, 2001). The transition from thickening to extension is marked by a regional phase of strike-slip deformation, which is bracketed between the Late

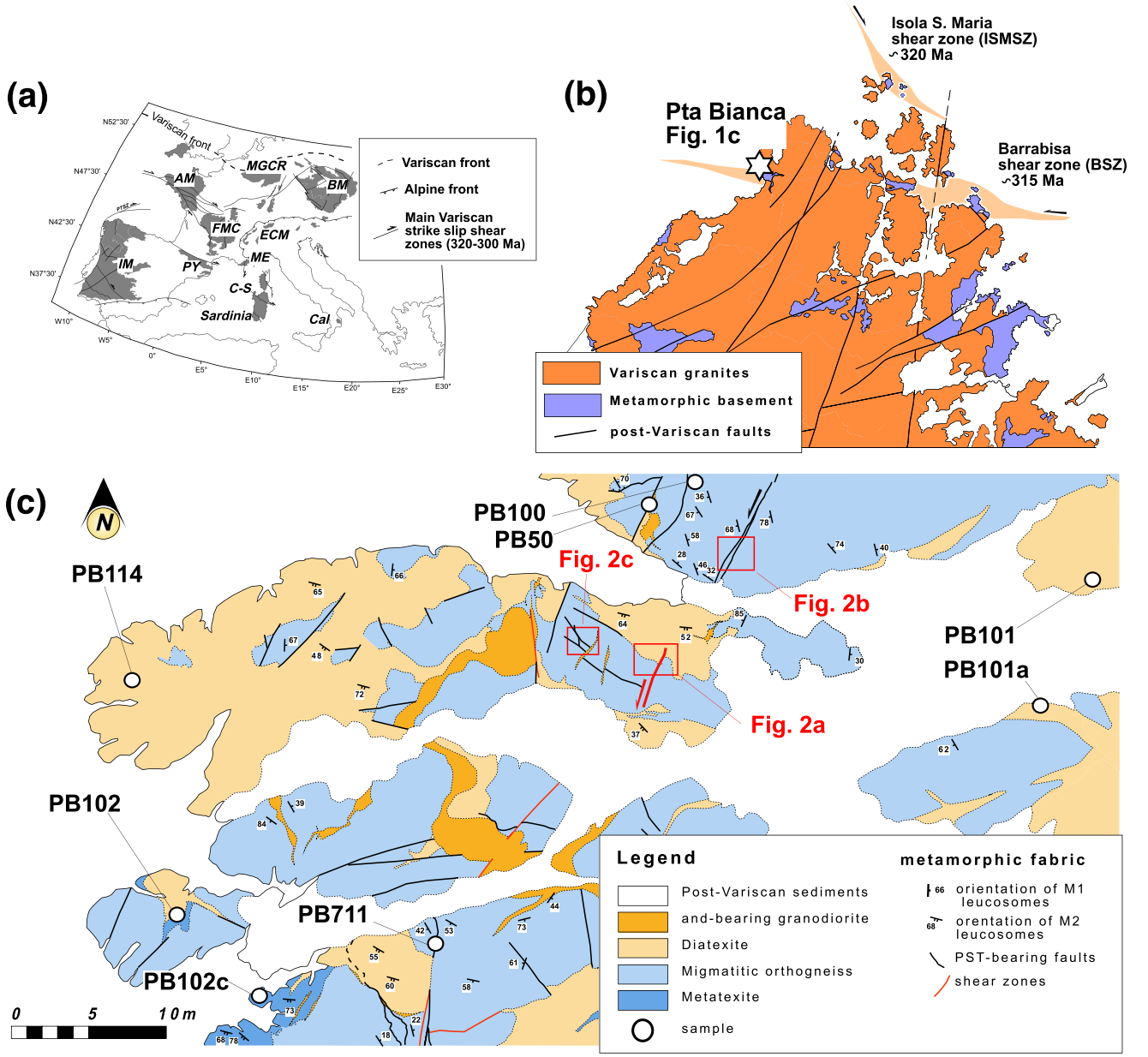

FIGURE 1 Geological setting: (a) distribution of the principal Variscan domains in central and southern Europe (AM, Armorican Massif, IM, Iberian Massif, PY, Pyrenees, FMC, French Massif Central, C-S, Corsica–Sardinia block, Cal, Calabria, ECM, External Crystalline Massifs of the Alps, BM, Bohemian Massif, MGCR, Mid-German Crystalline Rise, ME, Maures-Esterel); (b) simplified geological map of NE Sardinia, the white star marks the position of the studied area; the age of Isola *S. Maria* and Barrabisa shear zones are from Padovano et al. (2014), this work, respectively; (c) structural map of the study area, the position of selected samples is indicated. [Colour figure can be viewed at wileyonlinelibrary.com]

Mississippian and the Early Permian in the southern part of the chain and also in the French Massif Central and the Armorican Massif (Carosi et al., 2012; Gébelin et al., 2009; Martínez Catalán, 2012; Matte, 2001; Rolin et al., 2009). The Corsica–Sardinia Block (Figure 1a) presents an almost complete section of the chain, from the non-metamorphic fold-and-thrust belt in SW Sardinia to the high-grade, mainly migmatitic, orogenic root zone exposed in NE Sardinia and Corsica. Petrologic evidence indicates that partial melting in northern Sardinia begins in the kyanite stability field ($P = 0.7$–1.3 GPa, $T = 680$–750°C), in response to the onset of post-collisional exhumation of the thickened Variscan crust and evolved under lower pressure conditions in the sillimanite/andalusite stability fields (Cruciani et al., 2001; Cruciani, Franceschelli, Elter, et al., 2008a; Giacomini et al., 2006, 2008; Massonne et al., 2013). The onset of anatexis is constrained by several methods to have occurred during the

early Carboniferous (340–350 Ma; Ferrara et al., 1978; Carmignani et al., 1994; Giacomini et al., 2006, 2008). Most authors agree that continuous decompression maintained supra-solidus conditions in the middle and lower crust until about 320 Ma, the age of the youngest anatectic melts in NE Sardinia and southern Corsica (Cruciani et al., 2019; Giacomini et al., 2008). The final stage of anatexis involved dehydration melting of biotite in the sillimanite stability field ($T = 650–690°C$, $P = 0.6–1.0$ GPa; Giacomini et al., 2005; Carosi et al., 2012), producing MgO- and K_2O-rich granodioritic melts that are interpreted as precursors of the Corsica–Sardinia Batholith (320–285 Ma; Casini, 2012; Casini et al., 2012, 20151,b; Rossi & Cocherie, 1991; Paquette et al., 2003). Thus, according to this interpretation, decompression of the Variscan crust was nearly isothermal (Cruciani et al., 2008a,b; Giacomini et al., 2005, 2008). The good match between the age of the youngest anatectic melts and that of late-Variscan *HT* shear zones in N Sardinia (Figure 1b), Corsica and Maures-Esterel massifs (315–325 Ma) has led some authors to suggest that the end of anatexis probably marks the switch from post-collisional extension to crustal shearing (Carosi et al., 2012; Casini, Cuccuru, Puccini, et al., 2015b; Casini & Funedda, 2014; Cuccuru et al., 2012; Edel et al., 2014; Padovano et al., 2014; Secchi et al., 2022).

2.2 | Local geology

The study area (Pta Bianca, Figure 1b) represents the western tip of a large-scale E-W shear zone (Barrabisa Shear Zone, BSZ) developed in north Sardinia during the final stage of anatexis, at the onset of regional shearing (Casini et al., 2015a,b; Padovano et al., 2014). In the present study, the migmatite terminology follows Sawyer (2008). The study area exposes a foliated, strongly peraluminous andalusite-bearing granodiorite and various types of migmatite characterized by a variable paleosome to neosome ratio (Figure 1c). Field relationships evidence two distinct generations of leucosomes, corresponding to different melting events labelled as M1 and M2 (Figure 2). Based on the total volume of leucosome, we distinguish migmatites with relatively low or high melt proportion, respectively, as metatexite (melt < 20 vol.%) and diatexite (melt > 30 vol.%) (Sawyer, 1999). A further distinction is introduced here to distinguish metatexite derived from sedimentary protoliths as metatexitic metapelite and those derived from calc-alkaline arc-related Ordovician plutons (460–475 Ma, Casini, Cuccuru, Oggiano et al., 2010; Puccini, et al., 2015b). In this latter case, we identify them as metatexitic orthogneiss.

3 | METHODS

3.1 | Sample collection and petrographic analysis

A total of 29 samples were collected from the metatexitic orthogneiss, metatexitic metapelite and diatexite. Around 15–20 kg of eight selected samples, three metatexitic orthogneiss containing pseudotachylyte veins (PB50, PB100 and PB711), two stromatic metatexite (PB102 and PB102c) and three diatexite (PB101, PB101a and PB114) were collected for whole rock chemical analyses. Samples were crushed and split to obtain representative fractions and pulverized in a tungsten-carbide mill. Chemical composition was determined at the Activation Laboratories (Ontario) by fusion ICP and fusion ICP-MS for major and trace elements, respectively (Table 1). The same samples were also used for microstructural observations on polished thin sections cut parallel to the XZ and YZ planes of the finite strain ellipsoid. Microprobe analyses were done for the main mineral phases. Representative electron microprobe analyses of plagioclase, K-feldspar, biotite (samples PB100, PB101 and PB101a) and garnet (PB101a) and cordierite (samples PB101, PB102) are summarized in Table 2. Values of the analyses with a total oxide % sum between 99 and 100.5 have been considered for feldspars and between 99 and 101% for garnet; for biotite we have only used those with values of total dry oxide % sum >95. Cordierite values have been included in the tables in spite that they are considered qualitative (as it was not fresh enough in samples PB101 and PB102). The values considered are those with a total dry oxide % sum >96.5. The analyses of samples PB100 and PB102 were carried out at the Centres Científics i Tecnològics of the Universitat de Barcelona using a Cameca SX-50 electron microprobe with a wavelength-dispersive spectrometer in point beam mode at 15 nA and 20 kV, with 10 μm beam diameter. The potential for calibration error was mitigated by recalibrating before each session against a range of natural and synthetic standards. Sample PB101 was analysed at the University of Milano with an electronic microprobe JEOL JXA-8200 using an accelerating voltage of 15 kV, an electron beam current of 7.5 nA and a beam diameter of 5 μm. Microprobe analyses were converted to molecular mineral formulae using a standard number of oxygen atoms per formula unit (Deer et al., 1966). Biotite cations and proportion of Fe^{3+} in biotite were determined using the method described in Will (1998). Garnet was classified using the spreadsheet by Locock (2008). In spite that it calculates 29 endmembers, for the studied samples, only alm, prp, grs and sps are significant (>0.05%). Mineral abbreviations used are ms, muscovite; qtz, quartz; grt, garnet; crd, cordierite; sill, sillimanite; bt,

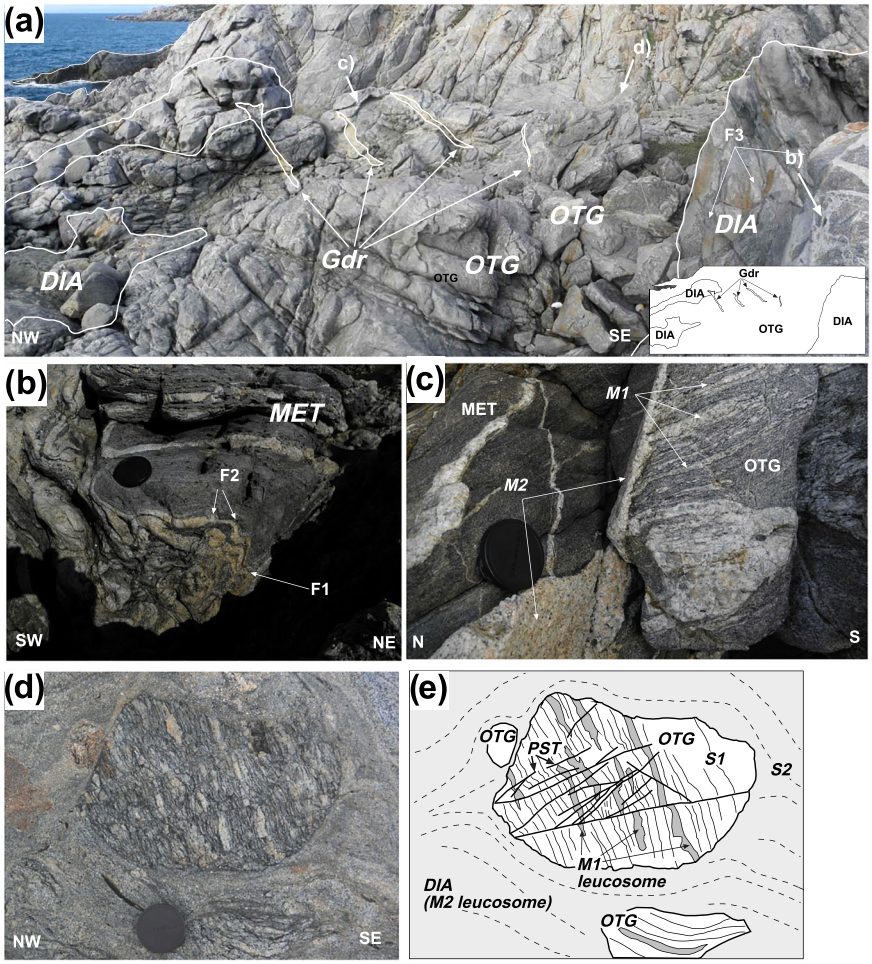

FIGURE 2 Field photographs: (a) field relationships between the metatexitic orthogneiss (OTG), diatexites (DIA) and granodioritic melt pockets (Gdr) related to the late phase of M2 melting stage, (b) interference between F1 and F2 folds in leucosomes of metatexite (MET), (c) geometric relationships between M1 and M2 leucosomes, (d) detail of diatexite with clasts of metatexitic orthogneiss deformed by a dense network of thin pseudotachylytes, (e) line-drawing of Figure 2d; the S1 and S2 foliations are indicated by solid and dashed white lines, respectively; the thick white lines mark the pattern of pseudotachylytes (PST) preserved within the larger clast of metatexitic orthogneiss; M1 (dark grey) and M2 (light grey) leucosomes are also indicated. [Colour figure can be viewed at wileyonlinelibrary.com]

biotite; pl, plagioclase; kfs, K-feldspar; liq, silicate liquid; ilm, ilmenite; mt, magnetite; mnz, monazite; zrn, zircon; ap, apatite; An_{xx}, anorthite; X_{Mg} (grt, bi) = Mg/(Fe + Mg), X_{alm} = Fe/(Ca + Fe + Mg + Mn), X_{grs} = Ca/(Ca + Fe + Mg + Mn), X_{prp} = Mg/(Ca + Fe + Mg + Mn), X_{sps} = Mn/(Ca + Fe + Mg + Mn), X_{an} = Ca/(Ca + Na + K), X_{ab} = Na/(Ca + Na + K), X_{or} = K/(Ca + Na + K). apfu refers to the number of atoms per formula unit.

3.2 | Geochronological methods

Zircon and monazite U–Pb geochronology was performed by laser ablation–inductively coupled plasma–mass spectrometry (LA-ICP-MS) at the CNR-IGG of Pavia. Zircon grains from a pseudotachylyte-bearing metatexitic orthogneiss (sample PB100) and a M2 diatexitic leucosome (sample PB101) have been characterized and dated as mineral separates, while both zircon and monazite from pseudotachylytes were studied directly on thin sections collected from 1 to 2.5 cm thick vein (sample PB711). Zircon grains were separated using conventional methods (Wilfley table, magnetic separation and heavy liquid), handpicked under a binocular microscope and then mounted in epoxy resin. Textural position and internal features were investigated with a scanning electron microscope (SEM Mira3 Tescan), and cathodoluminescence (CL) images were acquired with a SEM Philips515 equipped with a Centaurus scintillator CL detector at the University of Pavia. Monazite grains were also characterized by quantitative chemical analyses (Si, P, S, Ca, Y, La, Ce, Pr, Nd, Sm, Eu, Gd, Dy, Pb, Th and U) and compositional maps (Y, Ce, Pr, Th, P, Ca, La, Nd, Sm, Gd) acquired using an electronic microprobe (JEOL JXA 8200, at the University of Milano).

The LA-ICP-MS system couples an ArF excimer laser microprobe at 193 nm (Geolas 102 MicroLas) with a sector field ICP–MS (Element from ThermoFinnigan). Analytical methods for zircon and monazite geochronology are fully described in Tiepolo (2003) and Paquette and Tiepolo (2007). Dating was performed following the analytical procedure suggested by Langone et al. (2011) and Maino et al. (2012, 2019). The signals of ^{202}Hg, $^{204}(Pb + Hg)$, ^{206}Pb, ^{207}Pb, ^{208}Pb, ^{232}Th and ^{238}U masses were acquired. The presence of common Pb is monitored by

TABLE 1 Major and trace element composition of selected samples

	PB100	PB50	PB711	PB101	PB101a	PB114	PB102	PB102c
SiO2 (wt%)	67.24	68.93	69.27	67.93	68.77	72.56	62.83	65.39
Al2O3	15.79	16.32	15.86	16.41	15.51	14.19	16.17	15.39
Fe2O3	4.78	3.19	2.53	4.5	3.94	1.79	6.56	5.41
MgO	1.58	0.079	1.17	0.58	0.59	0.57	2.28	1.94
CaO	2.7	1.15	2.54	2.69	3.04	1.92	1.71	3.97
Na2O	3.43	3.05	3.68	4.26	4.39	3.29	2.47	3.29
K2O	2.96	3.85	3.49	2.39	2.34	4.82	4.79	2.40
TiO2	0.455	2.26	0.43	0.274	0.35	0.27	0.91	0.88
MnO	0.077	0.406	0.05	0.082	0.06	0.02	0.112	0.06
P2O5	0.14	0.15	0.2	0.07	0.11	0.07	0.16	0.23
LOI	0.7	0.9	0.7	0.76	0.84	0.50	1.82	0.94
Total	99.84	100.3	99.92	99.95	99.94	100.00	99.82	99.90
Ni (ppm)	80	< 20	7	< 20	5	9	50	15
Co	14	5	6	3	5	5.00	14	12
Cr	50	< 20	11	< 20	<5	17	80	45
V	53	62	24	14	13	22	121	72
Sc	12	9	10	6	10	8	17	15
Cu	60	< 10	24	40	54	48	40	38
Zn	70	70	65	50	48	52	90	92
As	< 5	< 5	<5	< 5	<5	<5	< 5	<5
Ga	18	17	20	18	19	18	21	25
Pb	24	20	26	20	22	26	27	34
Sr	167	217	307	240	264	210	232	216
Rb	118	85	111	87	86	112	179	121
Ba	600	689	600	899	888	1,302	1,111	651
Zr	214	245	127	360	272	87	348	224
Nb	11	9	14	11	15	7	13	17
Ta	1.2	1	1.5	0.5	0.8	0.7	1.1	1.3
Mo	< 2	< 2	<2	< 2	<2	<2	< 2	<2
Th	11.5	13.3	6	7.9	9	13	17.4	20
U	2.2	4.5	< 5	1.8	< 5	5	4.3	6
Y	24	29	15	15	17	19	48	34
La	34.3	26.9	21.54	33.6	23.81	21.16	57.8	61.24
Ce	70.5	53.2	43.82	61	44.85	42.34	118	111.57
Nd	29.4	21.6	17.3	22.4	17.17	18.14	50.3	48.58
Sm	6	4.7	3.74	3.7	3.5	3.92	10.6	9.74
Yb	2.2	2.5	1.08	1.3	1.44	1.58	5.1	2.55
Eu	0.93	0.95	0.92	1.7	1.58	1.05	1.74	1.53
Pr	8.02	5.88	6.1	6.39	2.98	5.12	13.2	12.5
Gd	5.1	4	3.23	2.8	3.1	2.96	8.9	7.68
Tb	0.8	0.7	0.7	0.4	0.5	0.6	1.4	1.8
Dy	4.3	3.7	2.41	2.1	2.26	2.76	8.3	5.67

(Continues)

TABLE 1 (Continued)

	PB100	PB50	PB711	PB101	PB101a	PB114	PB102	PB102c
Ho	0.8	0.7	1.1	0.4	0.4	0.3	1.7	1.6
Er	2.1	2.2	1.17	1.2	1.46	1.61	5.1	3.12
Tm	0.32	0.35	0.36	0.18	0.21	0.25	0.78	0.9
Be	5	3	3	3	2.5	2.8	2	2.2
Ge	1	2	1	< 1	1	<1	1	1
Ag	0.7	< 0.5	0.6	1.3	1.5	1.6	1	1
In	< 0.2	< 0.2	<0,2	< 0.2	<0,2	<0,2	< 0.2	<0,2
Sn	3	3	4	3	4	3	4	3
Sb	< 0.5	< 0.5	<0,5	< 0.5	<0,5	<0,5	< 0.5	<0,5
Cs	9.4	4.2	4.4	4.1	7.92	6.3	7.9	6.6
Lu	0.36	0.41	0.18	0.22	0.29	0.26	0.77	0.46
Hf	5.3	5.9	5.2	7.3	8.79	7.8	8.7	7.4
W	20	< 1	12	16	15	15	15	14.0
Tl	0.7	0.5	0.6	0.5	0.95	0.78	0.9	0.85
Bi	< 0.4	< 0.4	<0,4	< 0.4	<0,4	<0,4	< 0.4	<0,4

the net signal of ^{204}Pb (subtracted for the isobaric interference of ^{202}Hg and background). Remarkably, the signal of ^{204}(Pb + Hg) is always indistinguishable from the background in the investigated samples. However, the relatively high Hg signal in the gas blank does not exclude the effective presence of common Pb in the analysed grains. The ^{235}U signal was calculated from ^{238}U based on the ratio $^{238}U/^{235}U = 137.818$ (Hiess et al., 2012). U–Pb fractionation effects in zircon and monazite were simultaneously corrected for using a matrix matched external standard and considering the same integration intervals on the standard and the unknowns. Analytical conditions vary from 10 μm diameter of spot size, 8 J cm^{-2} of energy density and 3 Hz of repetition rate for monazite, while for spot sizes of both 10 and 20 μm, a repetition rate of 5 Hz and a laser fluence of 8 J cm^{-2} were used with zircons. The instrumental and laser-induced U–Pb fractionations were standardized to the reference zircon GJ-1 (609 Ma; Jackson et al., 2004) as external standard, and the reference zircons 91,500 (1065 Ma; Wiedenbeck et al., 1995) and/or 02123 (295 Ma; Ketchum et al., 2001) were selected as validation standards. Monazite analyses were corrected using the reference Moacir monazite as external standard (Gasquet et al., 2010; Seydoux-Guillaume et al., 2002). The reproducibility of the standards was numerically propagated through all age determinations according to the equation of Horstwood et al. (2003). Only the analyses satisfying this procedure are considered accurate to within the quoted errors. The relative standard deviation of the analyses is mostly between 1 and 3%. Data reduction was carried out with the GLITTER® software (van Achterberg et al., 2001). Data processing and plotting were done with ISOPLOT/Ex (Ludwig, 2003). Results and reference materials are reported in Tables S1 and S2 in the supporting information. All errors on the final U–Pb ages for zircons and monazites reported in the main text are given at the 2σ level.

3.3 | Thermodynamic modelling

Thermodynamic modelling was carried out for a diatexite and a metatexitic metapelite (samples PB101 and PB102), using Theriak-Domino software (version 15.r187-gf; Capitani & Petrakakis, 2010) and ds62 dataset (Holland & Powell, 2011; February 2012 upgrade) adapted to Theriak Domino by D.K. Tinkham (td-tcds62-6axmn-03). Pseudosections were performed in the chemical system MnO–Na_2O–CaO–K_2O–FeO–MgO–Al_2O_3–SiO_2–H_2O–TiO_2–O (MnNCKFMASHTO). Fluid, if present, is considered to be pure H_2O. The modelling used the a-x relationships of White et al. (2001) and White, Powell, Holland, et al. (2014a) for melt (liq); Green et al. (2012) and White et al. (2014a, b) for orthopyroxene (opx), biotite (bt) and garnet (grt); Holland and Powell (2011), White, Powell, Holland, et al. (2014a) and Smye et al. (2010) for muscovite (ms); Powell et al., 2014 and White, Powell, & Johnson, 2014b for chlorite (chl); Holland and Powell (2003) for plagioclase (pl) and K-feldspar (kfs); Holland and Powell (2011) and White

et al. (2014a, 2014b) for cordierite; White et al. (2002) for magnetite-spinel (mag-spl); and White et al. (2000) and White, Powell, and Johnson (2014b) for ilmenite-haematite (ilm-hem).

Despite the rocks having experienced two melting episodes, we assume that the system was water saturated at the onset of M2 melting episode because it followed pseudotachylyte formation at sub-solidus PT conditions. M2 melting was probably triggered by fluids drained within the shear zone because of the increase of dynamic porosity related to the seismic event testified by pseudotachylytes (see below). Thus, in the models, H2O content is set to just saturate the wet solidus with a free fluid phase, but the system becomes fluid-absent immediately above it. For the modelled samples, the estimated amount of water is 3.27 mol.% (0.76 wt%) for sample PB101 and 3.28 mol.% (1.82 wt%) for sample PB102.

Following the approach of Diener and Powell (2010) and Rebay et al. (2010), we investigated the influence of changes in Fe^{3+} content in the modelled assemblages. On the basis of the best fit between observed and modelled assemblages (in particular opaque ore assemblages) and textural relations, we converted an amount of 13% of $Fe2^{+}$ to Fe^{3+} in each sample, leading to addition of 0.24 (PB101) and 0.35 (PB102) mole percent of extra oxygen in the modelled bulk composition.

4 | STRUCTURAL ANALYSIS

4.1 | Field observations

Both types of metatexites show a pervasive migmatitic fabric marked by thin (2–50 mm thick) stromatic leucosomes related to an early melting stage M1 (Figure 2b,c). These M1 leucosomes are parallel to a N-S to NNW-SSE-trending S1 foliation axial planar of strongly asymmetric, tight to isoclinal folds generally rootless and rarely observed in the field (Figure 2b). The quartz-feldspathic leucosome alternate with biotite selvedges (1–2 mm thick) oriented parallel to S1 foliation. Kinematic indicators such as asymmetric K-feldspar porphyroclasts, sigma-type objects and bookshelf structures are commonly observed within the metatexitic metapelite, indicating a top-to-the W sense of shear.

The migmatitic fabric defined by M1 leucosomes is displaced by a dense network of fractures and faults establishing a clear relative chronology (Figure 2d,e). The main faults are steep and roughly oriented NNE–SSW; however, several conjugate structures, oriented WSW-ENE and NW-SE can be observed (Figure 1c). The fault zones generally consist of a fine-grained highly deformed core (0.5–5 cm thick) that evolves to a densely fractured damage zone (1–50 cm thick) locally injected by thin (2–15 mm thick) pseudotachylyte veins.

Both the M1 migmatitic fabric and pseudotachylytes are, in turn, deformed by E-W ductile shear zones associated to the development of an S2 foliation and asymmetric F2 folds oriented NW to WNW-ESE (Figure 1). In places, the S2 foliation transposes the S1 fabric (Figure 2b,d). The shear zones are frequently injected by quartz + plagioclase + K-feldspar + biotite + garnet ± cordierite granodioritic leucosomes, apparently related to a second melting stage M2 (Figure 2d,e). In places, the volume and connectivity of these garnet-bearing M2 leucosomes increase abruptly, such that the rock loses its typical stromatic structure and becomes a diatexite. Diatexite domains are characterized by high neosome to paleosome ratio, generally above 0.3, and a dominantly magmatic structure. They incorporate variable proportions of metatexite and amphibolite fragments. Relicts of the older migmatitic fabric, mostly stromatic leucosomes and the pervasive S1 foliation, are still recognizable within the largest fragments of metatexitic orthogneiss (Figure 2d,e).

4.2 | Microstructure

4.2.1 | Metatexitic orthogneiss

Overall, this metatexite has a gneissic-granoblastic microstructure formed by quartz and feldspar, 5–10 mm thick leucosomes, alternating with 0.5–1 mm biotite-bearing melanosomes (Figure 3a). The rock is composed by qtz + $An_{21–41}$ pl + bt ± kfs. Common accessory minerals include ilmenite, apatite, zircon, monazite and titanite; ilmenite occurs associated with biotite.

Large quartz and feldspar crystals show evidence for intracrystalline deformation and are generally bounded by sub-grains with serrated to lobate boundaries (Figure 3b). Quartz forms pockets and incipient ribbons. Bigger crystals exhibit undulose extinction defining the typical chessboard pattern characteristic of *HT* mylonite and magmatic rocks (Krhul, 1996). More deformed crystals exhibit a core–mantle microstructure with a gradual transition between sub-grains and completely recrystallized new grains. Plagioclase and K-feldspar are idiomorphic to xenomorphic. They are essentially devoid of intracrystalline deformation features, except for stress-twins and rare sub-grains localized at feldspar–feldspar contacts. They preserve, in places, a magmatic fabric and show limited evidence for crystal-plastic deformation and *HT*-recovery. Biotite occurs as large (200–500 μm) elongated flakes that have a strong Shape Preferred Orientation (SPO) defining a gneissic

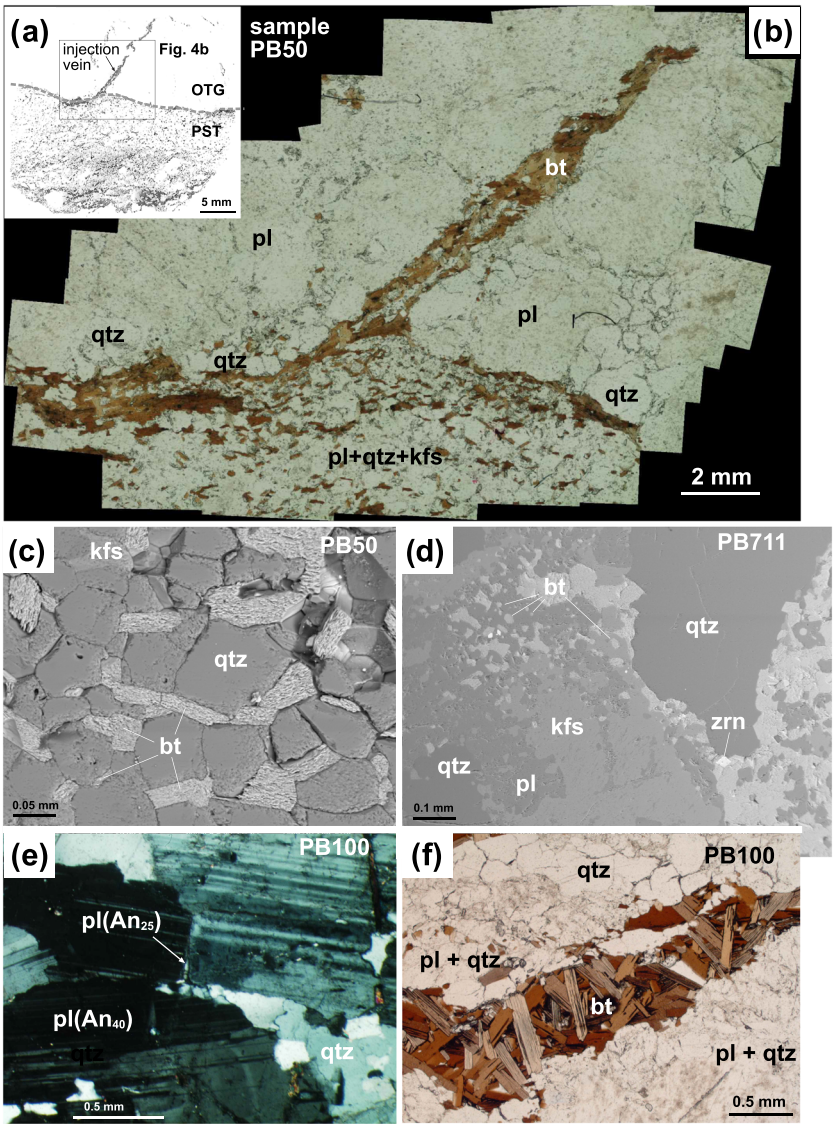

FIGURE 3 Microstructure of the metatexitic orthogneiss: (a) aspect of a thick recrystallized pseudotachylyte vein (PST), (b) biotite-rich injection vein transitioning to a thick recrystallized pseudotachylyte vein composed of a fine-grained aggregate of quartz + plagioclase k-feldspar + biotite, (c) Backscattered diffraction (BSD) image of recrystallized pseudotachylyte matrix, (d) rounded biotite crystals within pseudotachylyte matrix (BSD), (e) relatively residual domain of the metatexitic orthogneiss showing corroded plagioclase (An_{40}) and incipient M1 leucosome forming interstitial aggregates of more sodic plagioclase (An_{25}) and quartz, (f) injection vein filled by large biotite crystals perpendicular to the fracture walls. [Colour figure can be viewed at wileyonlinelibrary.com]

foliation parallel to the stromatic M1 leucosomes. Leucosomes are mostly formed by quartz, plagioclase and K-feldspar in variable proportions. Pseudotachylytes are quite common within the metatexitic orthogneiss. They mostly consist of fragments of migmatite embedded within a crypto-crystalline matrix formed by qtz +- kfs + pl ± bt filling a network of fractures. In places, biotite-rich injection veins branching off the main slip surfaces can be observed (Figure 3c,d). The composition of biotite in pseudotachylyte veins is similar to that in the metatexite (Table 2a).

4.2.2 | Metatexitic metapelite

Metatexites derived from pelitic gneisses (sample PB102) are medium- to fine-grained rocks with a distinctive layered microstructure consisting of thin (1–5 cm thick) stromatic M1 leucosomes alternating with thicker (2–15 cm thick) biotite-rich melanosomes. The boundaries between stromatic leucosomes and melanosomes are generally marked by a local increase of biotite yielding to the development of thin selvedges (Figure 4a). Both the leucosomes and the melanosomes are roughly parallel to the regional S1 foliation recognized in the field. The S1 foliation is defined by trails of sillimanite and biotite needles occasionally preserving nearly isoclinal, rootless, F1 folds (Figure 4b). The M1 leucosomes (mean grain size 2–4 mm) have a quite homogeneous assemblage composed of qtz + pl ± kfs ± bt (Figure 4a). The melanosomes (mean grain size (0.5–3 mm) consist of variable proportions of bt + qtz + $An_{21–41}$ pl + kfs ± sill. Cordierite is scarce (around 1–2 vol.%) and generally forms in between leucosomes and melanosomes. It may include fibrolitic sillimanite (Figure 4c). Common accessory minerals include zrn + mnz + ilm ± mt ± ap (Figure 4d). Finally,

TABLE 2A Mineral composition: Representative microprobe mineral analyses of biotite from Punta Bianca

Sample	Orthogneiss PB-100			Diatexite PB-101			Metatexite PB-102	
Analysis number (wt%)	b2–68	b2–113	b2–138	4B-an101	4B-an105	4Ban111	i-37	i-39
SiO_2	35.48	34.79	35.13	32.76	32.92	32.88	35.04	34.85
TiO_2	2.97	2.78	3.11	2.38	2.26	2.44	3.8	3.47
Al_2O_3	18.56	17.84	17.82	21	20.75	20.31	18.19	18.59
FeO (total)	19.51	20.47	19.88	27.54	27.28	27.38	20.09	20.26
FeO ($^{2+}$)[a]	16.58	17.40	16.90	23.41	23.19	23.27	17.08	17.22
Fe_2O_3[a]	3.25	3.41	3.31	4.59	4.55	4.56	3.35	3.38
MgO	8.58	8.82	8.92	3.39	3.48	3.60	7.90	7.88
MnO	0.36	0.36	0.36	0.40	0.23	0.19	0.28	0.32
CaO	0.07	0.01	0.01	0.00	0.00	0.00	0.01	0.00
Na_2O	0.15	0.26	0.24	0.14	0.28	0.30	0.22	0.28
K_2O	9.27	9.39	9.22	9.24	8.84	9.32	9.24	9.19
Sum (dry)	95.27	95.06	95.01	97.30	96.50	96.88	95.11	95.18
Number of ions on the basis of 11 O ignoring H_2O								
Si	2.69	2.67	2.68	2.53	2.55	2.55	2.67	2.66
Al^{IV}	1.31	1.33	1.32	1.47	1.45	1.45	1.33	1.34
Al^{VI}	0.35	0.28	0.29	0.44	0.45	0.41	0.31	0.33
Ti	0.17	0.16	0.18	0.14	0.13	0.14	0.22	0.20
Fe^{2+}	1.05	1.12	1.08	1.51	1.50	1.51	1.09	1.10
Fe^{3+}	0.19	0.20	0.19	0.27	0.27	0.27	0.19	0.19
Mg	0.97	1.01	1.02	0.39	0.40	0.42	0.90	0.90
Mn	0.02	0.02	0.02	0.03	0.02	0.01	0.02	0.02
Sum VI	2.75	2.79	2.77	2.78	2.77	2.76	2.73	2.74
Ca	0.01	0.00	0.00	0.00	0.00	0.00	0.00	0.00
Na	0.02	0.04	0.03	0.02	0.04	0.05	0.03	0.04
K	0.90	0.92	0.90	0.91	0.88	0.92	0.90	0.89
Sum A	0.92	0.96	0.93	0.93	0.92	0.97	0.93	0.94
Sum cations	7.68	7.74	7.71	7.71	7.69	7.73	7.66	7.68
Si/(Si +Al IV)	0.67	0.67	0.67	0.63	0.64	0.64	0.67	0.66
Mg/(Mg+Fe 2+)	0.48	0.47	0.48	0.21	0.21	0.22	0.45	0.45

muscovite crystals commonly associated with chlorite overgrowths of biotite and pinnite alteration of cordierite are interpreted as retrograde products formed by sub-solidus cooling.

4.2.3 | Diatexite

Diatexites (sample PB101) are highly heterogeneous rocks composed of a medium-grained neosome domain (mean grain size 0.5–2 mm) enveloping a myriad of paleosome fragments derived from M1 metatexites of various composition. The most common assemblage observed within M2 neosomes is qtz + $An_{7–29}$ pl + kfs + bt + grt ± crd, although garnet and cordierite are very scarce, less than 1 vol.%. Accessory minerals generally include zircon + monazite ± xenotime ± titanite (Figure 5a). The composition of diatexite is quite variable on a local scale because of the large variation in biotite, garnet and cordierite content that may result into the development of a magmatic layering defined by alternating quartz-depleted schlieren diatexite and more felsic quartz + plagioclase + K-feldspar ± biotite bands (White et al., 2005). The SPO of idiomorphic biotite crystals

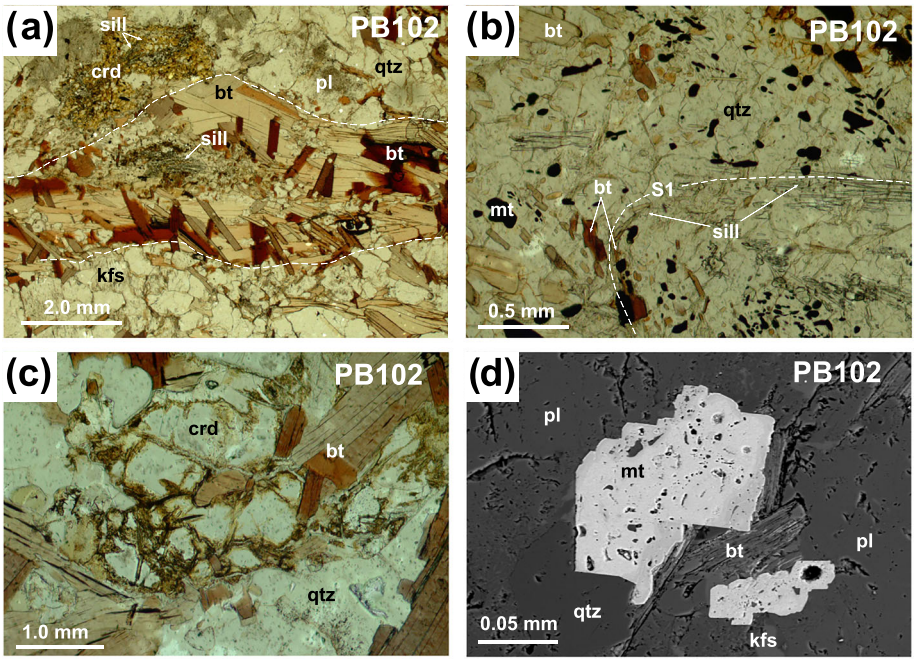

FIGURE 4 Microstructure of metatexitic metapelites: (a) biotite-rich selvedge (marked by dashed white lines) bounded by quartz + plagioclase melanosomes; note the large cordierite crystal overgrowing sillimanite on the upper left corner of the image, (b) detail of a rootless fold marked by the biotite + sillimanite S1 foliation, (c) close-up of a fractured, largely pinnitized, cordierite crystal, (d) backscattered diffraction (BSD) image of magnetite [Colour figure can be viewed at wileyonlinelibrary.com]

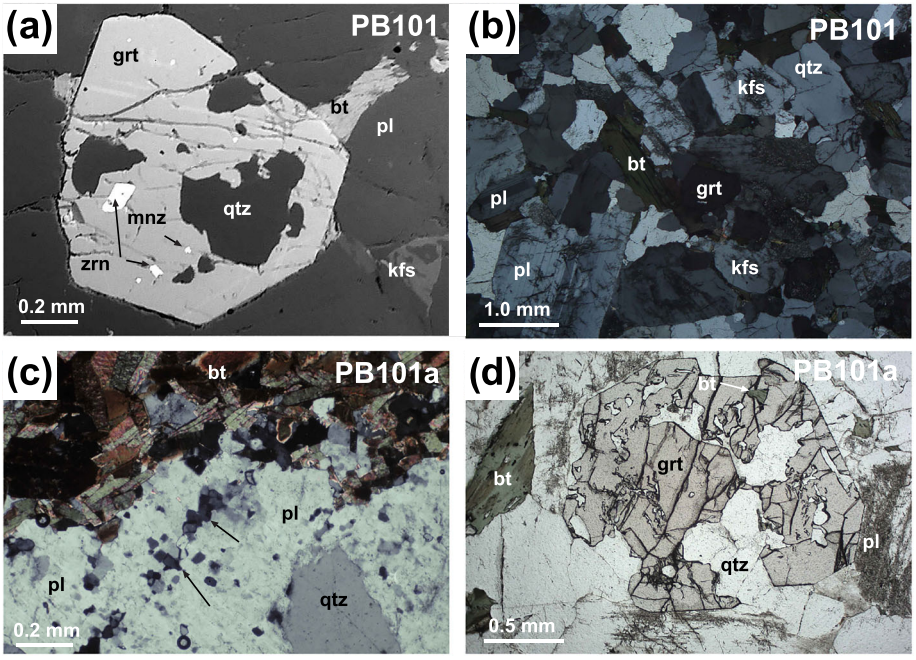

FIGURE 5 Microstructure of diatexite: (a) backscattered diffraction (BSD) image of a small idiomorphic garnet containing several inclusions of monazite and zircon, (b) biotite-rich layer showing a well-marked magmatic flow foliation parallel to the regional S2, (c) boundary between a residual biotite-rich fragment and M2 leucosome; the black arrows mark an incipient microshear zone developed at plagioclase–plagioclase contact, (d) large (>1.5 mm across) garnet crystal partly corroded and replaced by quartz and biotite. [Colour figure can be viewed at wileyonlinelibrary.com]

marks a locally well-developed magmatic flow foliation parallel to the regional S2, which is generally consistent throughout all compositionally distinct layers (Figure 2b,d). Plagioclase and K-feldspar are generally sub-idiomorphic to interstitial, though in places they are partly corroded with oscillatory zoning and Carlsbad twinning (Figure 5b). Quartz is usually interstitial and shows extensive evidence for *HT* crystal-plastic deformation such as chessboard pattern, sub-grains and incipient intra-granular shear zones composed of recrystallized new grains. All other minerals show limited evidence for crystal-plastic deformation, such as mirmeckyte and rare sub-grains at plagioclase–plagioclase contacts (Figure 5c). Strongly pinnitized cordierite forms small, sub-idiomorphic, crystals within the quartz-K-feldspar matrix. Garnet forms small (0.2–2.8 mm across), clean and nearly idiomorphic crystals with rounded inclusions of biotite and K-feldspar. Some garnets, particularly larger crystals (>1 mm), are partly corroded and replaced by quartz + biotite pseudomorphs (Figure 5d).

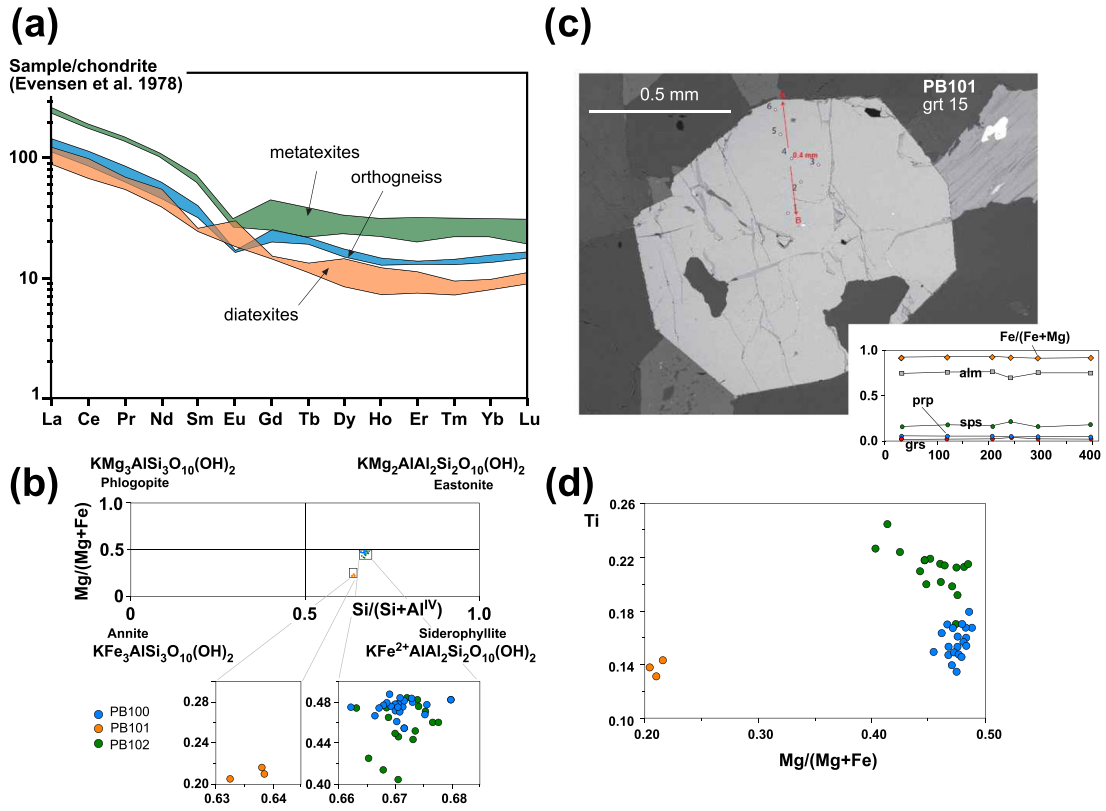

FIGURE 6 Geochemical and compositional data: (a) cumulative REE patterns of different migmatite types normalized after Evensen et al. (1978), (b) composition of biotite, (c) representative compositional profile of garnet from sample PB102, (d) Ti content of biotite of all samples. [Colour figure can be viewed at wileyonlinelibrary.com]

5 | WHOLE ROCK COMPOSITION

The bulk composition of the selected migmatite samples is provided as weight percent of oxides (wt%) in Table 1. Overall, both types of metatexite are quite similar, with SiO_2 content varying in a narrow range between about 67–71 and 62–68 wt% and the Mg/(Mg + Fe) ratio between 0.24–0.30 and 0.25–0.26, respectively (Table 1). Diatexite samples show somewhat more variable composition with SiO_2 ranging between 67 and 75 wt% and a Mg/(Mg + Fe) ratio between 0.11 and 0.25 (Table 1). However, the largest chemical variation in diatexite appears to be the proportion between refractory, relatively immobile, components (Fe_2O_3 + MgO + TiO_2) and more mobile elements such as Na_2O + K_2O. The former likely increase in melt-depleted domains that are enriched in paleosome fragments, whereas the latter generally concentrate in neosomes (e.g. Guernina & Sawyer, 2003; Milord et al., 2001; Sawyer, 1998). Samples PB101b and PB114 have low to intermediate neosome to paleosome proportion ($M = 0.35$–0.5) and are characterized by an elevated ratio of $Na_2O + K_2O > 8.1$ wt%. The other diatexite sample, PB101a, has much higher neosome proportion ($M > 0.75$) and lower $Na_2O + K_2O$ content of about 6.6 wt% (Table 1). All samples have quite similar contents of trace elements, although Th, Ba, Zr and Rb are generally more concentrated within metatexitic metapelite than in the metatexitic orthogneiss and diatexite samples. All samples are characterized by nearly flat HREE patterns and substantial enrichment in LREE. Both types of metatexite show similar REE patterns characterized by negative Europium anomaly. Metatexites derived from pelitic protholith are relatively more enriched in REE, though. The compositional variability of diatexite is reflected also by trends in the pattern of REE (Figure 6a). In fact, the samples with lower leucosome proportion (PB101 and PB114) show moderately positive to absent Europium anomaly, whereas diatexite with largest leucosome proportion (PB101a) is characterized by a more positive Europium anomaly (Figure 6a).

6 | MINERAL CHEMISTRY

The mineral chemistry of the three different types of migmatite is presented in the remainder of this section. The composition of representative minerals is given in Table 2.

6.1 | Metatexitic metapelite

Biotite from all microstructural domains, that is, neosome and paleosome, is siderophyllite with an intermediate Mg/(Mg + Fe) ratio (0.4–0.5) and relatively low Al content (17.5–18.5 wt%) (Figure 6b,d and Table 2a). There is no correlation between Mg/(Mg + Fe) and Si/(Si + AlIV). Plagioclase is generally quite homogeneous with minor and non-systematic differences between the domains. It is characterized by oligoclase-andesine composition (An_{25}–An_{36}) with very low orthoclase content (Or_0–$Or_{1.8}$). K-feldspar is generally perthitic with variable albite content between Ab_{11} and Ab_{18} (Table 2b). Cordierite is strongly pinitized. A few relicts preserved within larger porphyroblasts have intermediate to high Mg/(Mg + Fe) ratio (0.53–0.59) and variable Na2O content (0.24–0.67 wt%) recalculated on a basis of 18 oxygens (Table 2).

6.2 | Metatexitic orthogneiss

Biotite is quite homogeneous in all microstructural domains of the metatexitic orthogneiss (Table 2a). Significant parameters as Si/(Si + AlIV) and Mg/(Mg + Fe) are 67.08 and 47.66, respectively, for the bigger biotite crystals from the metatexitic orthogneiss (Table 2a). The Ti content is systematically high (0.1–0.2 atoms per formula unit, a.p.f.u., based on a 11 oxygen atom normalization) and shows a slight linear negative correlation with the Mg/(Mg + Fe) ratio (Figure 6b,d). The high Ti values indicate greater amount of Ti solid solution at high metamorphic temperatures (Faye, 1968; Forbes & Flower, 1974; Robert, 1976) and are considered by Henry and Guidotti (2002) as characteristic of high-grade zones. Plagioclase is slightly variable and has oligoclase-andesine composition (An_{21} to An_{41}). Its content in Or (Or_0–Or_2) is generally very low (Table 2b). K-feldspar is generally perthitic with variable albite content between Ab_8 and Ab_{19} and absent or very low anorthite (Table 2a).

6.3 | Diatexite

Biotite is siderophyllite with intermediate Al_2O_3 content (19.8–23.7 wt%) in all microstructural sites (Figure 6a), that is, the magmatic matrix and the rounded inclusions occasionally preserved within large garnets. These latter crystals have a generally lower Mg/(Mg + Fe) ratio (0.19–0.20) compared with the matrix biotite (Mg/(Mg + Fe) ratio = 0.21–0.23), yet there is still no obvious correlation between Mg/(Mg + Fe) and Si/(Si + Al^{IV}). The Ti content is quite high (0.13–0.15 a. p. f. u.) as observed in biotites of the metatexitic orthogneiss (Figure 6d; Table 2a). Plagioclase is generally quite heterogeneous with strong compositional variations between different domains. It is characterized by mean albite-oligoclase composition (An_7–An_{29}) with high orthoclase content ($Or_{2.0}$–$Or_{29.1}$). K-feldspar is generally perthitic with variable albite content between $Ab_{3.7}$ and $Ab_{11.2}$ (Table 2b). Cordierite is completely pinnitized. Garnet has a mean composition of almandine 73–83 wt%, pyrope 3–5 wt%, spessartine 10–20 wt% and grossular 2–4 wt% (Table 2c). The Mg/(Mg + Fe) ratio is mostly constant around 0.95 (Figure 6d). The small idiomorphic garnets are generally homogeneous from core to rim, yet their composition can vary between different crystals (Figure 6c). By contrast, the large (width > 1.5–2.0 mm) partly corroded garnets show a weak compositional zonation characterized by core to rim increase in almandine, from 73 to 83 wt%, and a slight decrease of spessartine from 20 to about 11–12 wt%. Pyrope and grossular are generally very low and do not show any significant variation from core to rim and from one crystal to another. Fifteen garnets were analysed; the profile of garnet 15 is shown (Figure 6c). In general, garnets have quite flat profiles although they register variable almandine core values ranging from $X_{alm} = 0.73$–0.82 and constant rim values around $X_{alm} = 0.82$. Pyrope values are constant in cores and rims, being $X_{prp} = 0.03$ in the core and $X_{prp} = 0.04$–0.05 in the rims. Spessartine values are variable in the core and range between $X_{sps} = 0.10$–0.20 and constant in the rims ($X_{sps} = 0.11$–0.12). Grossular content does not vary in the core and the rim showing values between $X_{grs} = 0.02$–0.04.

7 | P–T CONDITIONS

7.1 | Forward modelling

P–T pseudosections were calculated for a metatexitic metapelite (PB102), a metatexitic orthogneiss (PB100) and a diatexite (PB101) in the range 0.1–0.6 GPa and 600–1000°C. In this section, only pseudosections PB101 and PB102 will be described as pseudosection for sample Pb100 is similar to that of PB102 and gives no relevant additional data. We have used the sample's bulk composition as the primary control on its equilibrium phase relationships as the model reproduces the mineral assemblages observed in thin sections, the mode and quite satisfactorily the mineral compositions. In Figures 8 and 9, plagioclase and ilmenite are in excess. Quartz is in excess except where indicated (−qtz).

Compositionally, samples PB101 and PB102 have similar content of Al_2O_3 and MnO. Sample PB101 is richer in

TABLE 2B Mineral composition: Representative microprobe mineral analyses of feldspars from Punta Bianca

Sample (wt%)	Orthogneiss PB-100								Diatexite PB-101		
	Ksp	Pl							Ksp		
Analysis number	74	61	62	63	64	65	66	67	4B-an112	4B-an113	4B-an114
SiO_2	64.84	61.83	60.48	60.14	59.70	60.15	59.91	59.11	63.73	63.78	63.38
TiO_2	0.02	0.02	0.01	0.00	0.02	0.01	0.02	0.00	0.00	0.00	0.10
Al_2O_3	18.33	23.24	24.05	24.68	24.85	24.59	24.88	25.45	19.36	19.19	18.94
FeO	0.02	0.09	0.03	0.00	0.03	0.02	0.02	0.02	0.03	0.03	0.02
MgO	0.03	0.00	0.04	0.04	0.00	0.00	0.00	0.00	0.05	0.08	0.06
MnO	0.01	0.01	0.00	0.02	0.02	0.02	0.02	0.03	0.02	0.00	0.00
CaO	0.07	5.17	6.00	6.56	6.81	6.78	6.97	7.50	0.02	0.00	0.00
Na_2O	2.13	8.59	8.25	7.85	7.93	7.85	7.68	7.42	0.40	0.35	0.27
K_2O	13.67	0.30	0.22	0.33	0.34	0.34	0.25	0.19	16.11	16.26	16.26
Sum	99.11	99.33	99.08	99.65	99.76	99.76	99.76	99.73	99.72	99.70	99.04
Number of ions on the basis of eight O											
Si	3.00	2.76	2.72	2.69	2.67	2.69	2.68	2.65	2.96	2.96	2.96
Ti	0.00	0.00	0.00	0.00	0.00	0.00	0.00	0.00	0.00	0.00	0.00
Al	1.00	1.22	1.27	1.30	1.31	1.30	1.31	1.34	1.06	1.05	1.04
Fe^{2+}	0.00	0.00	0.00	0.00	0.00	0.00	0.00	0.00	0.00	0.00	0.00
Mn	0.00	0.00	0.00	0.00	0.00	0.00	0.00	0.00	0.00	0.00	0.00
Mg	0.00	0.00	0.00	0.00	0.00	0.00	0.00	0.00	0.00	0.01	0.00
Ca	0.00	0.25	0.29	0.31	0.33	0.32	0.33	0.36	0.00	0.00	0.00
Na	0.19	0.74	0.72	0.68	0.69	0.68	0.67	0.64	0.04	0.03	0.02
K	0.81	0.02	0.01	0.02	0.02	0.02	0.01	0.01	0.95	0.96	0.97
Sum cations	5.00	5.00	5.01	5.01	5.02	5.01	5.01	5.01	5.01	5.01	5.01
Mol per cent end members											
$NaAlSi_3O_8$ (Ab)	0.1908	0.7377	0.7046	0.6715	0.6656	0.6642	0.6565	0.6347	0.0359	0.0320	0.0246
$CaAl_2Si_2O_8$ (An)	0.0034	0.2454	0.2832	0.3101	0.3159	0.3170	0.3292	0.3545	0.0009	0.0002	0.0001
$KAlSi_3O_8$ (Kfs)	0.8058	0.0169	0.0122	0.0183	0.0185	0.0188	0.0143	0.0108	0.9632	0.9677	0.9753

TABLE 2B (Continued)

Sample (wt%)	Diatexite PB-101					Metatexite PB-102				
	Ksp		Pl			Pl				
Analysis number	4B-an115	4B-an116	4B-an119	4B-an120	4B-an123	g-4	g-22	i-26	i-33	h-45
SiO_2	64.09	64.24	62.56	62.81	63.62	68.13	59.59	60.60	60.67	60.58
TiO_2	0.06	0.08	0.00	0.00	0.00	0.01	0.02	0.01	0.01	0.03
Al_2O_3	19.31	18.87	23.48	23.46	23.13	19.19	25.09	23.89	24.20	24.15
FeO	0.13	0.08	0.05	0.16	0.05	0.01	0.12	0.15	0.06	0.08
MgO	0.10	0.08	0.04	0.06	0.05	0.02	0.02	0.02	0.00	0.00
MnO	0.06	0.00	0.04	0.01	0.03	0.01	0.04	0.00	0.01	0.00
CaO	0.07	0.01	4.01	4.09	3.91	0.66	7.22	6.20	6.57	6.57
Na_2O	0.42	0.75	8.81	8.57	8.87	11.70	7.64	8.18	8.09	7.91
K_2O	16.11	15.61	0.68	0.55	0.60	0.16	0.19	0.12	0.32	0.24
Sum	100.35	99.72	99.68	99.71	100.26	99.90	99.93	99.17	99.93	99.57
Number of ions on the basis of eight O										
Si	2.96	2.97	2.78	2.79	2.81	2.99	2.66	2.72	2.71	2.71
Ti	0.00	0.00	0.00	0.00	0.00	0.00	0.00	0.00	0.00	0.00
Al	1.05	1.03	1.23	1.23	1.20	0.99	1.32	1.26	1.27	1.27
Fe^{2+}	0.00	0.00	0.00	0.01	0.00	0.00	0.00	0.01	0.00	0.00
Mn	0.00	0.00	0.00	0.00	0.00	0.00	0.00	0.00	0.00	0.00
Mg	0.01	0.01	0.00	0.00	0.00	0.00	0.00	0.00	0.00	0.00
Ca	0.00	0.00	0.19	0.19	0.18	0.03	0.35	0.30	0.31	0.31
Na	0.04	0.07	0.76	0.74	0.76	0.99	0.66	0.71	0.70	0.69
K	0.95	0.92	0.04	0.03	0.03	0.01	0.01	0.01	0.02	0.01
Sum cations	5.01	5.00	5.00	4.99	4.99	5.02	5.01	5.01	5.01	5.00
Mol per cent end members										
$NaAlSi_3O_8$ (Ab)	0.0376	0.0683	0.7681	0.7657	0.7765	0.9614	0.6501	0.6999	0.6782	0.6762
$CaAl_2Si_2O_8$ (An)	0.0035	0.0007	0.1932	0.2019	0.1892	0.0299	0.3395	0.2932	0.3044	0.3104
$KAlSi_3O_8$ (Kfs)	0.9589	0.9311	0.0387	0.0323	0.0343	0.0087	0.0104	0.0069	0.0174	0.0134

TABLE 2C Mineral composition: Representative microprobe mineral analyses of garnet from Punta Bianca

Sample (wt%)	Diatexite PB-101			
Analysis number	**4B-an97**	**4B-an100**	**4B-an104**	**4B-an108**
SiO_2	36.35	36.39	35.78	36.29
TiO_2	0.00	0.05	0.00	0.05
Al_2O_3	21.66	21.17	21.82	21.35
FeO (total)	35.88	36.71	36.65	36.07
Fe_2O_3 (calc)	0.67	0.31	0.96	0.00
MgO	1.14	1.12	1.27	1.14
MnO	4.72	4.13	3.93	4.33
CaO	0.93	0.89	0.63	0.85
Na_2O	0.07	0.00	0.01	0.00
K_2O	0.00	0.00	0.00	0.00
Sum (dry)	101.41	100.77	101.06	100.09
Number of ions on the basis of eight cations and 12 anions				
Si	2.94	2.96	2.92	2.96
Ti	0.00	0.00	0.00	0.00
Al	2.07	2.03	2.10	2.05
Fe^{2+}	2.39	2.48	2.44	2.46
Fe^{3+}	0.04	0.02	0.06	0.00
Mg	0.14	0.14	0.15	0.14
Mn	0.32	0.28	0.27	0.30
Ca	0.08	0.08	0.06	0.07
Na	0.01	0.00	0.00	0.00
K	0.00	0.00	0.00	0.00
vac.	0.01	0.01	0.01	0.02
Sum cations	8.00	8.00	8.00	8.00
Mol per cent end members				
Almandine	0.7963	0.8260	0.8130	0.8198
Pyrope	0.0459	0.0453	0.0513	0.0463
Spessartine	0.1079	0.0948	0.0904	0.0997
Grossular	0.0241	0.0198	0.0157	0.0182
Mg/(Fe+Mg)	0.0544	0.0520	0.0594	0.0535

Note: Thermodynamic background and petrological applications. Springer, Lecture Notes in Earth Sciences, 71, 315 pp.
[a]Calculated following Will, Th. M. (1998) Phase Equilibria in Metamorphic Rocks.

SiO2, CaO and Na_2O, whereas sample PB102 is richer in MgO, FeO, TiO_2 and K_2O. This results in similar pseudosections with the solidus line at around 735–740°C at 0.1 GPa and 675–680°C at 0.3 GPa. Nevertheless, the small differences in composition give a wider stability field of K-feldspar towards higher temperature in sample PB102 and the widening of cordierite and sillimanite stability fields to higher pressure. By contrast, in sample PB101 garnet stabilizes towards lower pressure.

Thus, the inferred peak M2 assemblage present in sample PB101 (qtz + pl + kfs + bt + grt +crd+ ilm ± mt) is stable in a wide super-solidus field in the diagram from 0.1–0.5 GPa and between 700 and nearly 800°C, where this assemblage coexists with liquid. The andalusite/sillimanite-in and the cordierite-out lines intersect the H_2O-out line, just above the solidus at 0.25 GPa. The absence of aluminosilicate in the sample and the scarce cordierite constrains the pressure conditions of PB101 at around 0.25–0.3 GPa. The mean analysed X_{Fe} value of biotite in the sample ($X_{Fe} = 0.79$) fits quite well with the calculated isopleths at 0.3 GPa near the solidus ($X_{Fe} = 0.76$). In the models, garnet is absent at 0.25 GPa

and 680°C but increases up to 3 vol% at 750°C at the same pressure (Figure 7). This amount of garnet is consistent with the scarce presence of garnet in the samples. Values of cordierite have not been compared as no good analyses have been obtained. Composition of analysed K-feldspar ($X_K = 0.93–0.98$) and plagioclase ($X_{Na} = 0.77$) correspond to retrograde sub-solidus temperature, whereas the isopleth composition at the solidus is (X_K kfs = 0.73) for K-feldspar and (X_{Na}ab = 0.70) for plagioclase. The inferred peak M1 assemblage present in sample PB102 (qtz + pl + kfs + bt + sill + ilm + mt) occupies a narrow P–T field between 0.32–0.6 GPa and 660–735°C, where this assemblage is in equilibrium with liquid. This field is bounded by the solidus line at around 0.3 GPa and 780°C. Under the microscope, sillimanite is wrapped by cordierite and by a second generation of biotite corresponding to a peak M2 assemblage qtz + kfs + bt + crd, which indicates that the path evolved from a higher-pressure field containing sillimanite + biotite to a lower pressure field with stable cordierite and K-feldspar at no more than ~740°C. Biotite composition as shown by the isopleths is $X_{Mg} = 0.40$, and the values are quite constant at a wide range of pressures and temperatures (Figure 8). The composition of biotite analysed at the microprobe ranges between $X_{Mg} = 0.40–0.49$. The lower value ($X_{Mg} = 0.40$) can correspond to the composition of non-retrogressed biotite frozen at solidus, whereas $X_{Mg} = 0.40–0.49$ can be explained by different degrees of retrogression of biotite at sub-solidus conditions. Mineral composition of analysed plagioclase (X_{Na}ab = 0.65–0.71) is quite variable. The lower (X_{Na}ab = 0.65) value fits the solidus composition of plagioclase predicted by the model (Figure 8), whereas the higher values can correspond to altered sub-solidus plagioclase. The composition of analysed K feldspar ($X_K$ksp = 0.82) may also correspond to sub-solidus T conditions ($T < 600$°C; Figure 8).

As a whole, we can interpret that the mineral assemblages reacted with a fluid phase and retrogressed them. Despite that values of analysed cordierite are not included in the tables because cordierite is highly altered, its X_{Mg} (from 0.55–0.59) corresponds to sub-solidus compositions; thus, it can indicate retrogression as also suggested by biotite and feldspar composition. The presence of magnetite in the assemblage is restricted to lower pressure at low oxidation state, and it widens towards higher pressure in a more oxidized environment. For the oxidation state used for the calculations, it becomes stable at a temperature above 710°C at 0.3 GPa and it is not stable at the solidus.

The two samples provide different conditions, suggesting that they are constraining different parts of the history of Punta Bianca massif. Sample PB102 registered a decompression and cooling path from the M1 melting stage ($P \sim 0.4–0.3$ GPa, $T \sim 750$°C–680°C; Figure 8) to below the temperature required for ductility of K-feldspar ($T < 600$°C) as testified by pseudotachylytes and other brittle structures. Decompression is followed by near-isobaric heating related to the M2 melting stage, as registered by the presence of sillimanite included in cordierite and by biotite mineral composition.

Conditions of metamorphism for sample PB101 can be constrained using garnet composition and mode providing information on the M2 melting stage and subsequent cooling history. Garnet mode increases with temperature up to 3.5 vol% at 750°C in the pseudosection (Figure 7). This is consistent with the small euhedral garnet crystals present in the sample. Comparison of garnet microprobe analyses with those predicted in the model (Figures 6c and 7) suggests a maximum temperature around 750°C as shown by almandine and spessartine isopleths. There is no clear evidence of melt loss; thus, sample PB101 would become melt absent at the solidus around 0.27 GPa and near 690°C following a nearly isobaric cooling path from peak temperature of about 750°C.

8 | GEOCHRONOLOGY

Zircon and monazite U-(Th-)Pb analyses were performed on the metatexitic orthogneiss, M2 diatexite and pseudotachylyte veins in order to constrain the relative chronology of the magmatic and deformation events. While the first anatectic event M1 is constrained between 365 and 340 Ma by mica $^{39}Ar/^{40}Ar$ and zircon U–Pb dating of syn-Variscan trondhjemitic leucosomes in northern Sardinia and southern Corsica (Del Moro et al., 1975; Ferrara et al., 1978; Giacomini et al., 2006), the second melting stage M2 detected in the study area needs to be dated. We collected samples from well-exposed outcrops in an area of about 1.5 km^2. Selected pseudotachylyte veins are located far from the younger leucosomes to avoid possible thermal disturbance.

8.1 | Metatexitic orthogneiss

Zircons from the metatexitic orthogneiss (sample PB100) are relatively homogeneous in size, ranging in length from 120 to 450 μm. They exhibit prismatic to short prismatic shapes as commonly observed in intrusive rocks (Corfu et al., 2003). The cores are generally rich in inclusions and appear either as structureless or characterized by complex zoning. Around the cores, typical magmatic overgrowths with oscillatory or sector zoning occur. Both

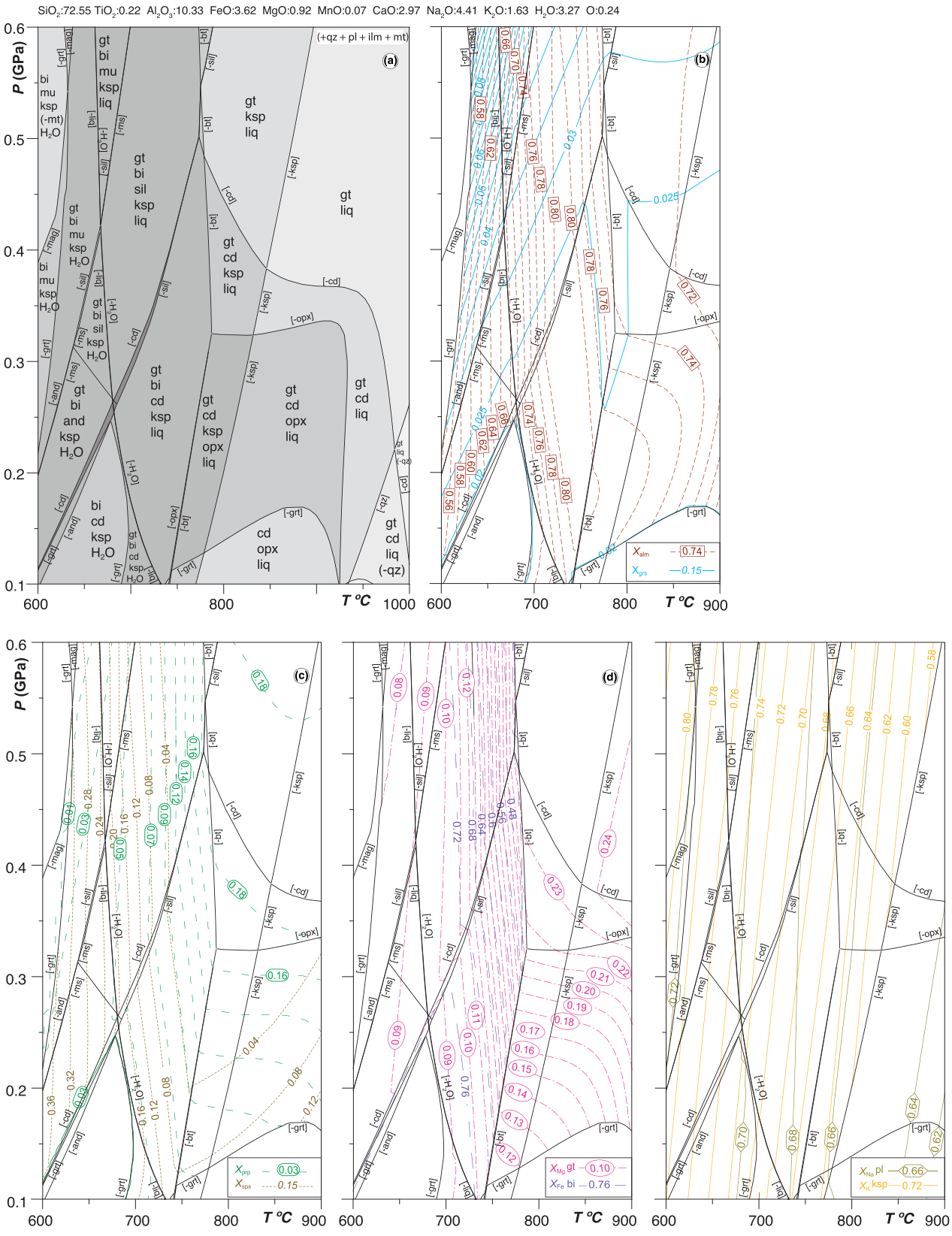

FIGURE 7 Thermodynamic modelling of sample PB101: (a) P–T pseudosection for sample PB101 in the system MnNCKFMASHTO, (b) almandine and grossular isopleths, (c) pyrope and spessartine isopleths, (d) X_{Mg} garnet and X_{Fe} biotite isopleths, (e) X_K pK-feldspar and X_{Na} plagioclase isopleths [Colour figure can be viewed at wileyonlinelibrary.com]

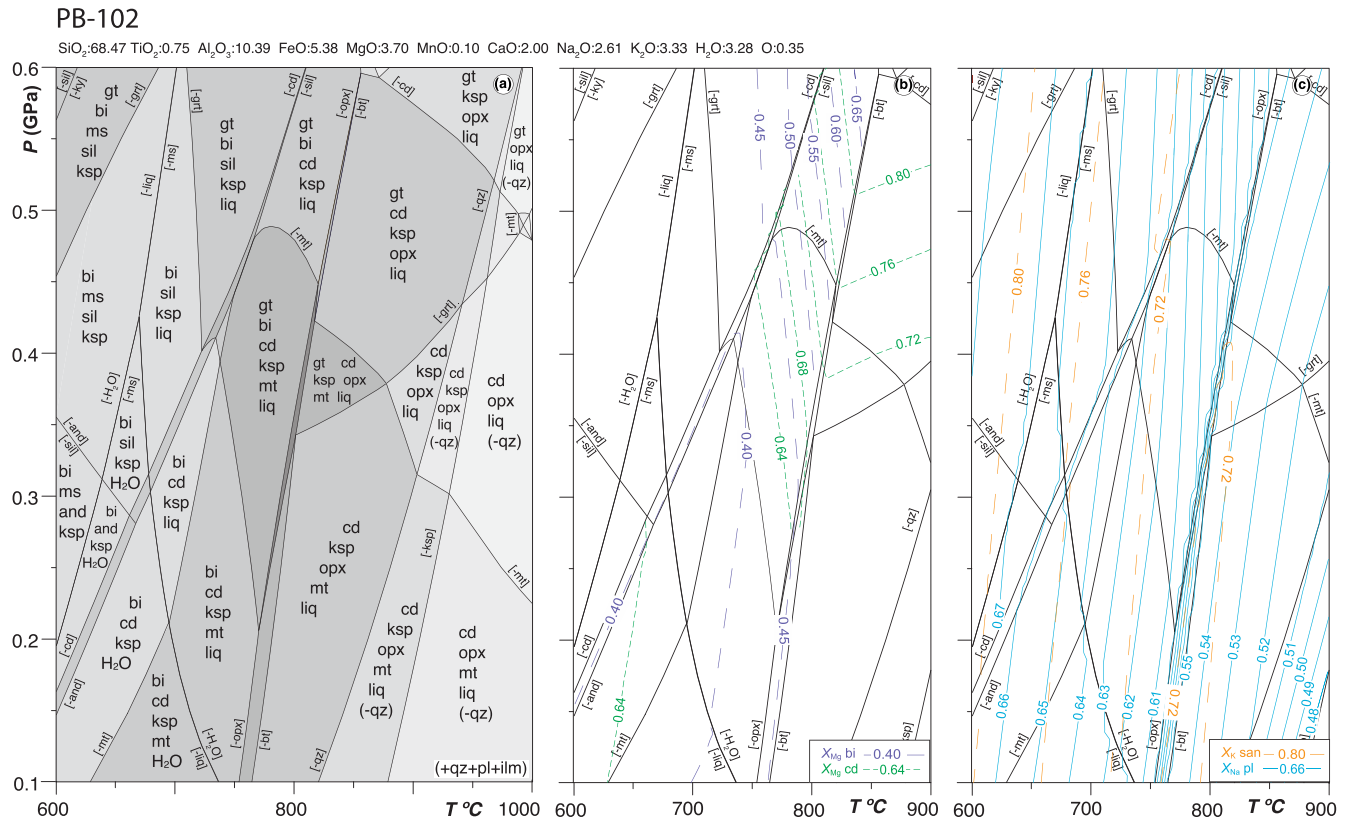

FIGURE 8 Thermodynamic modelling of sample PB102: (a) P–T pseudosection for sample PB102 in the system MnNCKFMASHTO, (b) X_{Mg} biotite and X_{Mg} cordierite isopleths, (c) X_K sanidine and X_{Na} plagioclase isopleths [Colour figure can be viewed at wileyonlinelibrary.com]

cores and magmatic overgrowths are commonly truncated or partially obscured by unzoned, poorly to highly luminescent homogeneous patches or resorption rims (Figure 9a–c). Thirty-seven analyses supplied 20 concordant data mostly ranging from 421 ± 13 to 491 ± 14 Ma apart from two isolated ages at 322 ± 10 and 556 ± 13 Ma. Cathodoluminescence images indicate that the oldest age encompasses an inherited core, whereas the youngest one is from a wide high-luminescent rim (Figure 9a–c). The data from the oscillatory or sector zoned domains yield a continuum spread of ages between 421 ± 13 and 491 ± 14 Ma with two main peaks around 470–485 and 440–460 Ma (Figure 10a,b).

8.2 | Diatexite

Zircon grains from diatexite (PB101) developed during the M2 melting stage are heterogeneous in shape and size (40–50 μm length). The common zircon structure consists of a xenocrystic core surrounded by an oscillatory or sector zoned domain (Figure 9d,e). Rims are generally narrow. The analysed sample provided 16 concordant data from 37 analyses. Spots on inherited cores yield the oldest ages between 488 ± 12 and 850 ± 31 Ma. The concordant data (43%) from the oscillatory-zoned domains show a scattered pattern of ages clustered around two main peaks:450–460 and 295–310 Ma (Figure 10c,e). The second population shows identical weighted mean age and mean U–Pb age of 302 ± 8 Ma (MSWD = 0.32; Figure 10d,e).

8.3 | Pseudotachylyte

8.3.1 | Zircon U–Pb results

Zircons from the pseudotachylyte veins (sample PB711) generally appear as small crystals or fragments (30–110 μm length), prismatic to rounded in shape and often fractured (Figure 9f,g). The common structure, made by xenocrystic cores, oscillatory overgrowth and rims, characterizes a few crystals, while most grains show a poor defined zonation partially or completely obscured by low to high luminescence patches or rims. Forty-one analyses performed on 32 minerals gave 21 concordant ages (51%) ranging from 599 ± 16 to 308 ± 10 Ma. Apart from two older ages from inherited cores

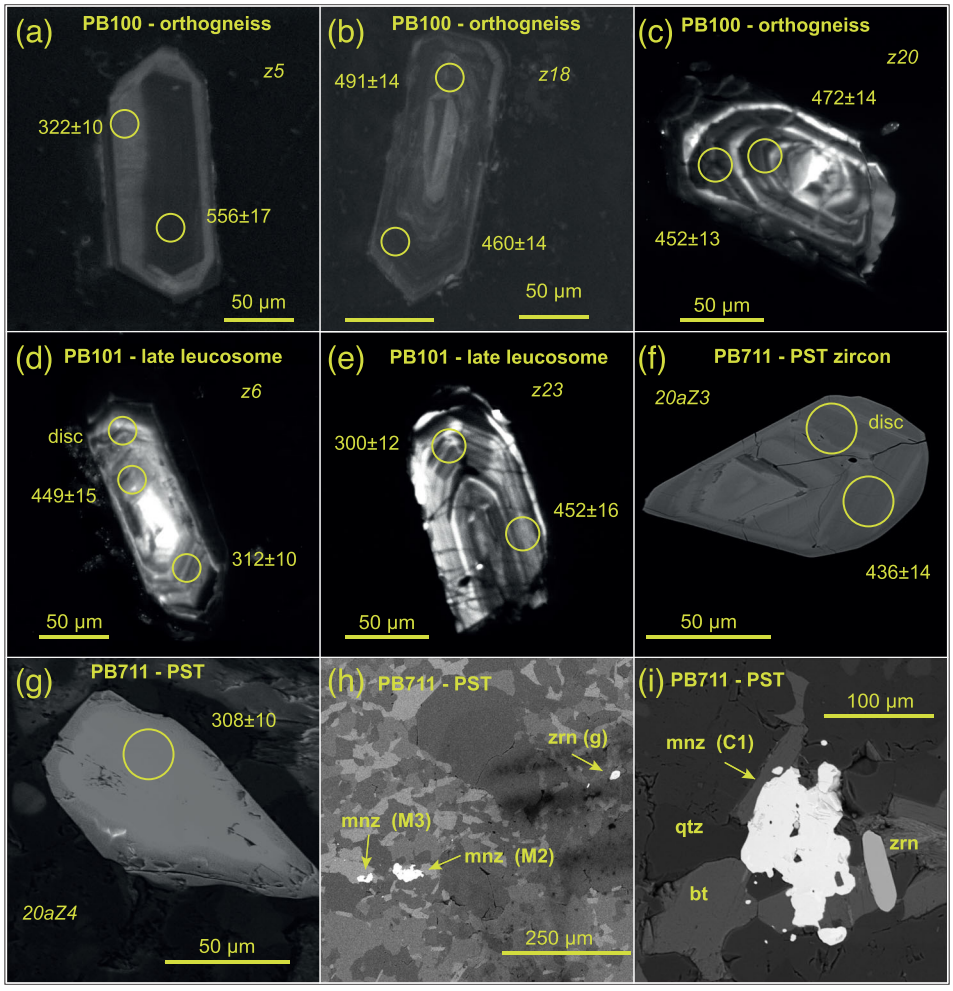

FIGURE 9 (a–g) Cathodoluminescence images of representative zircon grains from orthogneiss (sample PB100), diatexite (sample PB101) and pseudotachylyte (sample PB711). (h,i) Monazite in the recrystallized pseudotachylyte show sub-euhedral to irregular shape and triple junctions with the surrounding silicate minerals. Z# refers to the spot analysis in zircon grains, while M# and C# identify the analysed monazite grain (see Table S2 of the supporting information) [Colour figure can be viewed at wileyonlinelibrary.com]

(567 ± 16 and 599 ± 16 Ma), the other ages spread mainly between 420 and 470 Ma, followed by isolated ages at 308 ± 10, 327 ± 116, 380 ± 86 and 395 ± 9 Ma (Figure 10f,g).

8.3.2 | Monazite U-(Th)-Pb results

The pseudotachylyte contains abundant, tiny, rounded to elongated monazite grains, which are too small to be analysed. These crystals are commonly fractured by cracks and/or microcracks. However, some large monazite grains (up to 200 µm in length) show sub-idiomorphic to irregular shape and triple junctions between monazite and the surrounding silicate minerals (Figure 9h,i). Cracks are abundant and associated with bright BSE portions, commonly corresponding to high Th concentration (Figure 11a–d).

We performed quantitative chemical analyses and mapping on five large grains (Figure 11a–d and Tables S1 and S2). Monazite shows significant compositional variation in Y, Th and U contents. Y_2O_3 content is generally high (2.1–3.1 wt%) apart from narrow, irregular patches where it decreases at 1.8–1.1 wt%. ThO_2 content is highly variable from 2.5 to 22.2 wt%. Zones of high-Th concentration tend to have a patchy distribution and are mostly located in areas of weakness (cracks, crystal narrowing). UO_2 content is between 0.08 and 0.8 wt% and reaches the lowest values in Y-poor and Th-rich zone.

Eighteen analyses on six grains yielded six U–Pb concordant ages between 308 ± 11 and 337 ± 12 Ma (Figure 11e). Altogether, both concordant and discordant data yield ^{238}U-^{206}Pb ages between 291 ± 11 and 336 ± 12 Ma. The ^{232}Th-^{208}Pb data are decoupled from the ^{238}U-^{206}Pb data, and generally yield younger ages. Coupling the chemical mapping with the U–Pb data (Figure 11), we observe that the spot from a low-Y patch yields the oldest U–Pb age of 337 ± 12 Ma (^{238}U-^{206}Pb age of 336 ± 12 Ma). The other five U–Pb concordant ages from the large Y-rich zones are between 313 ± 12 and 308 ± 11 Ma. Discordant data from the same Y-rich domain show ^{238}U-^{206}Pb ages between 319 ± 12 Ma and 308 ± 12 Ma. Elemental distribution therefore indicates a main population characterized by high content of Y and

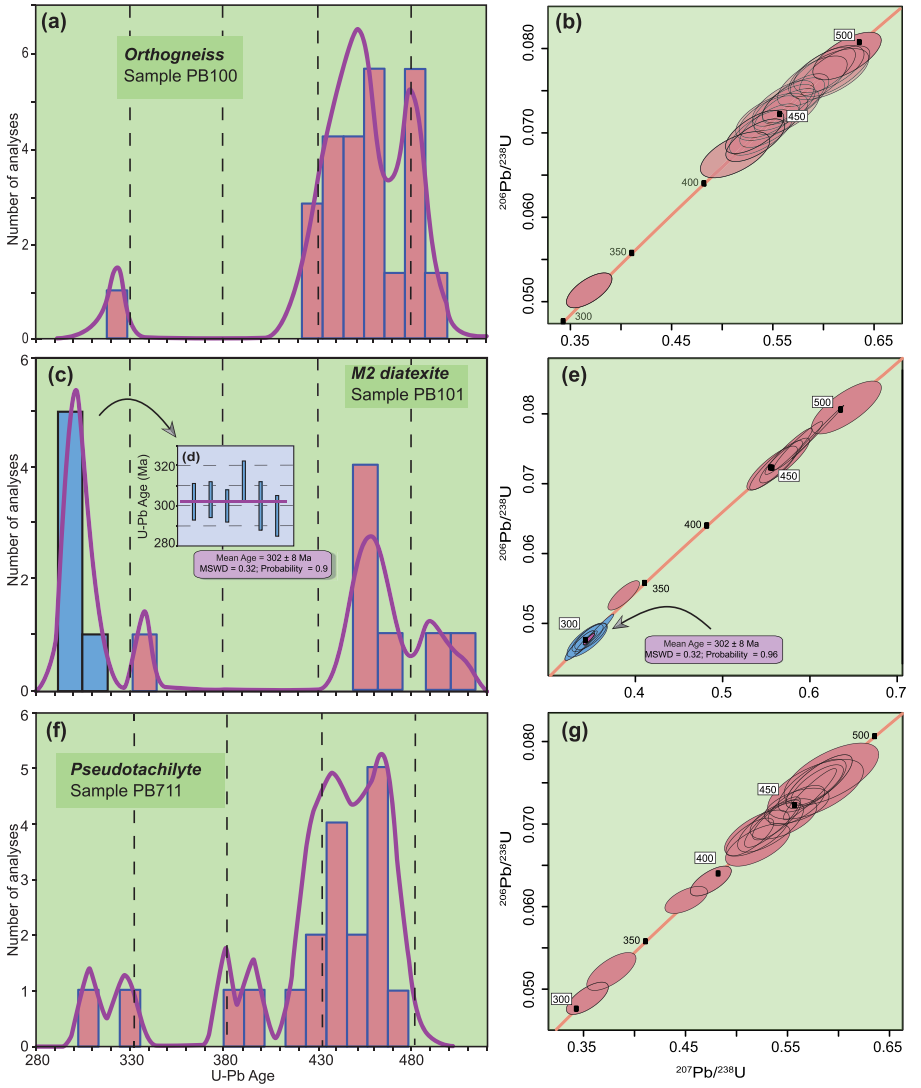

FIGURE 10 Probability density plots and U–Pb mean concordia ages for the zircon age resulting from metatexitic orthogneiss (a, b), M2 diatexite (c–e) and pseudotachylyte (f, g). Blue boxes/ellipses indicate the youngest population of the M2 diatexite. The inherited cores older than ~560 Ma are not plotted. [Colour figure can be viewed at wileyonlinelibrary.com]

moderate Th with a weighted mean U–Pb age of 310 ± 6 Ma (MSWD = 0.14) and a very similar ^{238}U-^{206}Pb age of 313 ± 4 Ma (MSWD = 0.32). The Tera–Wasserburg plot shows a consistent intercept age of 312 ± 5 Ma (MSWD = 0.09). Chemical mapping also shows that ^{238}U-^{206}Pb ages tend to decrease (between 299 ± 6 and 290 ± 6 Ma) where Th-rich patches are abundant (sample PB711). This time interval corresponds with most of the ^{232}Th-^{208}Pb data.

9 | DISCUSSION

9.1 | Zircon and monazite geochronology

It is widely known that zircon may (re)crystallize over a wide range of pressure and temperature conditions in response to melting, metamorphic reactions, hydrothermal activity or crystal-plastic deformation (e.g. Hoskin, 2005; Langone et al., 2018; Piazolo et al., 2012; Rubatto, 2002; Williams, 1992). Yet zircon commonly preserves the record of the crystal history throughout multiple magmatic and/or tectono-metamorphic stages providing a suitable method to investigate complex metamorphic and magmatic histories (e.g. Langone et al., 2017; Milan et al., 2016; Paterson et al., 1992; Spencer et al., 2017). Monazite has a very low lattice diffusion rate (Cherniak & Pyle, 2008), but fluid-enhanced dissolution–precipitation reactions can easily alter the chemical pattern of Y and REE as well as reset the U-Th-Pb systematics at relatively low temperatures (Harlov et al., 2011; Janots et al., 2006; Martins et al., 2009; Pyle & Spear, 2003). In such instances, monazite commonly shows spurious ages that are interpreted as caused by metamorphic reactions, mixed age or crystal-plastic deformation (e.g. Catlos et al., 2002; Erickson et al., 2015). In the following, we present an attempt to constrain the tectono-metamorphic evolution

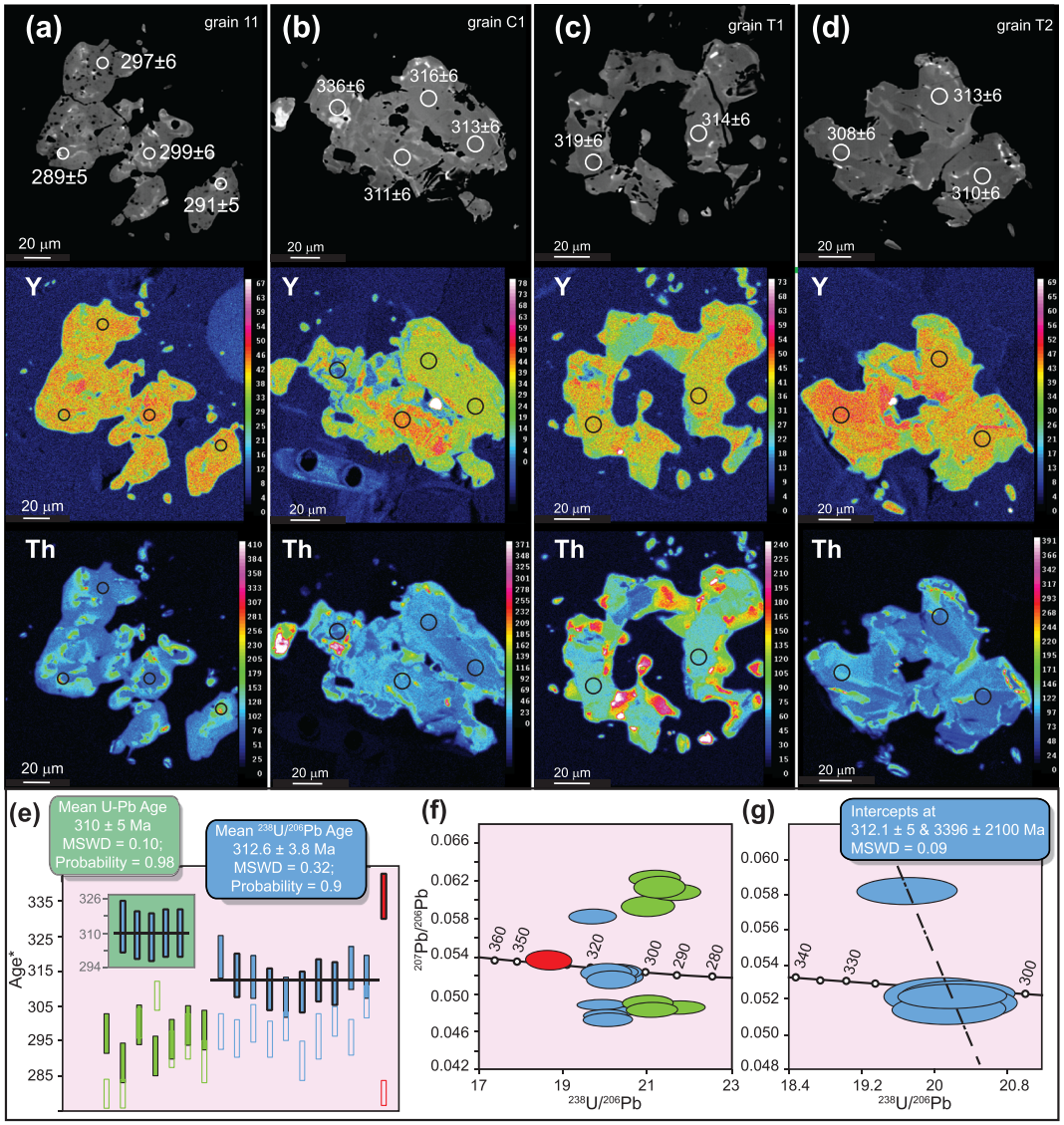

FIGURE 11 Backscattered images and X-ray elemental maps (Y and Th) of representative monazite grains; panels (a) to (d) refer to grains 11, C1, T1 and T2, respectively (see Table S2 in the supporting information). Analytical laser ablation spots of ~10 μm (white or black circles) and relative $^{206}Pb/^{238}U$ ages (with 1σ error) are reported. (e) $^{206}Pb/^{238}U$ (filled bars) and ^{232}Th-^{208}Pb (empty bars) ages are reported for three chemical domains: green indicates data from domains with high-Y and hogh-Th contents, red indicates low-Y and low-Th contents, blue represents high-Y and low to moderate Th domains. For this last population, mean $^{206}Pb/^{238}U$ (blu box) and U–Pb (green box) weighted ages are reported. (f,g): Tera–Wasserburg diagrams of the monazite U–Pb data divided as in (e); intercept reported in (g) has been calculated only for the age from high-Y and low to moderate Th domains (blue domain). [Colour figure can be viewed at wileyonlinelibrary.com]

of the studied rocks combining zircon and monazite U-Th-Pb geochronology.

9.1.1 | U–Pb zircon ages

In all samples, zircon U–Pb data (Table S1) show high percentage of discordant ages (between 45 and 60%), as well as large spreads of the concordant ages measured from the magmatic domains (i.e. oscillatory zoned overgrowth). As evidenced by numerous studies, these features are typical of inheritance or crystal-plastic deformation (e.g. Langone et al., 2018; Milan et al., 2016; Paterson et al., 1992; Piazolo et al., 2012, 2016; Spencer et al., 2017; Timms et al., 2017).

The age spread of the metatexitic orthogneiss (420–490 Ma) shows two main peaks around 470–485 and 440–460 Ma, which agree with the multiple episodes of Ordovician–Silurian magmatism documented throughout the Sardinia–Corsica block (Figure 12; Giacomini et al., 2006; Oggiano et al., 2010; Cocco et al., 2018). We thus infer that metatexites contain several generations of

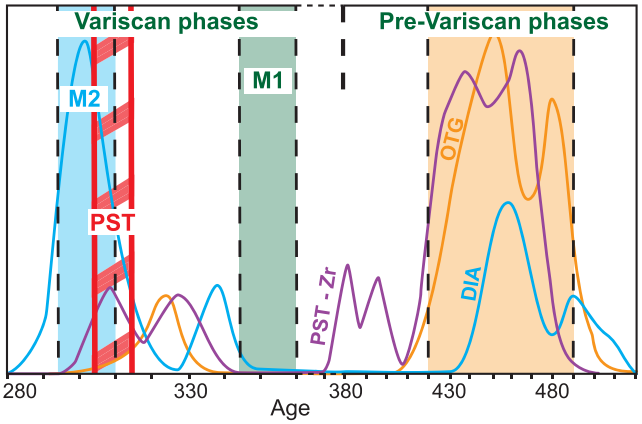

FIGURE 12 Geochronological data plotted within the tectonic framework of the Sardinia basement. Orange, blue and purple lines are the probability density plots of the metatexitic orthogneiss, diatexite and pseudotachylyte, respectively. The vertical blu, green and orange boxes indicate the time intervals of the magmatic events (M1 and M2) derived from geochronology (this work; Casini et al., 2015; Giacomini et al., 2006; Oggiano et al., 2010). The red striped box highlights the timing of the pseudotachylyte-forming event (PST). [Colour figure can be viewed at wileyonlinelibrary.com]

zircon crystallized during multiple pre-Variscan magmatic stages. The rim age of 322 ± 10 Ma likely reflects a partial isotopic resetting of the U–Pb system during Variscan metamorphism and deformation.

The diatexite also shows an old age population at 450–460 Ma, which corresponds to the Ordovician–Silurian age of the orthogneisses and therefore likely reflects inheritance. However, the younger population, with a weighted mean age of 303 ± 8 Ma, fits the late-Variscan age of M2 regional anatexis (Figure 12). The upper portion of this time interval agrees with the xenotime and monazite dissolution U–Pb ages (308 ± 2.8 and 313 ± 3.4 Ma, respectively) of equivalent granodioritic melts dated in the southern part of the study area (Casini, Cuccuru, Maino, et al., 2015a). The zircons separated from pseudotachylyte veins show a main population (420–480 Ma) indistinguishable from that of the metatexitic orthogneiss, and yield only few Variscan ages between 395 ± 9 and 308 ± 10 Ma (Figure 12).

9.1.2 | U-Th-Pb monazite age of pseudotachylytes

Monazite chemical analyses coupled with U-Th-Pb dating provide more information about the timing of pseudotachylyte development, providing robust constraints for the end of the M1 melting stage. Y-rich monazite domains generally crystallize after melting (Kohn, 2016; Kohn et al., 2005; Pyle & Spear, 2003), although typical Y-rich rims, mantling low-Y cores, may form during retrograde metamorphism (e.g. Gibson et al., 2004; Spear & Pyle, 2002). On the other hand, decrease of Y-content is generally related to prograde metamorphism because of competition with other phases, such garnet, allanite or xenotime (e.g. Spear & Pyle, 2010). Textures of the large monazite grains analysed in this work indicate coeval growth with the other silicate phases of the pseudotachylyte melt and provide homogeneous high-Y and moderate Th contents, typical of post-melting crystallization. A few low-Y domains, embodied within the larger portion of Y-rich crystals, likely represent metamorphic relicts that survived the M1 melting stage. U–Pb dating confirms a homogeneous age for the post-M1 Y-rich population (310 ± 6 Ma), whereas the single U–Pb age from the Y-poor domain is considerably older and possibly correlated to the main metamorphic stage (337 ± 6 Ma). Finally, the third chemical domain of monazite, characterized by both high-Y and high Th-contents, yields younger ^{238}U-^{206}Pb ages (<305 Ma, Figure 11). Noticeably, the ^{232}Th-^{208}Pb ages from all analyses show a shift towards the same time interval (c. 290–300 Ma). The monazite behaviour during melt crystallization is not completely understood, although significant increase of Th-content is not expected (Kohn et al., 2005; Stepanov et al., 2012). However, similar U-Th-Pb disturbances have been recognized in monazite affected by deformation or hydrothermal activity due to replacement by dissolution–precipitation fluid-mediated processes. Therefore, it seems plausible that the irregular to patchy distribution of Th-rich domains suggests a diffusion of Th along pathways characterized by fluid circulation during the late magmatic stage and/or deformation (Erickson et al., 2015; Grand'Homme et al., 2016; Seydoux-Guillaume et al., 2002). Th-rich patches are mostly associated with cracks, where the circulation of fluids may mobilize, carry and re-precipitate dissolved elements like Th and Pb.

9.1.3 | Age of metamorphic and tectonic events

Zircons within the metatexitic orthogneiss and diatexites retain two distinct age populations. The first, with ages roughly between 420 and 490 Ma, defines a broad Ordovician to Silurian peak. The latter corresponds to a late Carboniferous range (303–322 Ma). The Ordovician–Silurian peak is interpreted as the age of magmatic protholiths, widely preserved within the low grade metamorphic units exposed in southern-central Sardinia (Oggiano et al., 2010). On the contrary, the Carboniferous

ages preserved within the metatexitic orthogneiss reflect the onset of M2, which can be confidently constrained to the interval 303–313 Ma by combining zircon ages of diatexite (this study) and xenotime and monazite U–Pb dissolution ages (Casini, Cuccuru, Maino, et al., 2015a). The analysed samples retain only few ages related to the M1 melting stage. Yet the monazite age of pseudotachylyte-bearing faults indicates that the M1 melting stage is early Carboniferous (337 ± 12 Ma), as observed in other migmatitic massifs of northern Sardinia and southern Corsica (Ferrara et al., 1978; Giacomini et al., 2006, 2008).

9.2 | Metamorphic conditions

9.2.1 | M1 melting stage

The first melting stage, M1, can only be weakly constrained using pseudosection modelling in the study area. The maximum PT conditions recorded by sample PB102 ($P = 0.3$–0.6 GPa; $T = 660$–735°C) provide a reliable estimate of temperature, but the estimated pressure is lower than P estimates of 0.8–1.4 GPa from adjacent migmatitic massifs exposed in N Sardinia and southern Corsica (Figure 1; Cruciani et al., 2008; 2019; Fancello et al., 2018; Giacomini et al., 2006, 2008). Metamorphic conditions are generally not synchronous at the scale of an orogen and are expected to be also spatially variable (e.g. Burton & O'Nions, 1992). Yet the composition of protoliths, the metamorphic ages and the composition of M1-related leucosomes in the study area are strikingly like those from adjacent migmatitic massifs of northern Sardinia and southern Corsica (Cruciani et al., 2019; Giacomini et al., 2006, 2008). Moreover, these other massifs are close to the study area (<10 km apart) and there is no evidence for major tectonic discontinuities that can account for large vertical displacements and the juxtaposition of different structural levels (Casini, Cuccuru, Maino, et al., 2015a). Thus, we assume that the M1 stage occurred under PT conditions of 0.6–0.9 GPa and 700–720°C similar to those recorded in N Sardinia during the early Variscan phase of regional anatexis (Cruciani et al., 2016; Ferrara et al., 1978; Giacomini et al., 2006, 2008; Li et al., 2014).

9.2.2 | M2 melting stage

The quartz + plagioclase + k-feldspar + garnet + melt assemblage of sample PB101 is stable over a large T range, such that pseudosection modelling cannot accurately trace the super-solidus conditions recorded by the M2 melting stage (Figure 7; Pownall, 2015; Sawyer, 2020). Regardless of these uncertainties, the composition of coexisting garnet and biotite in equilibrium with melt corresponds to conditions of about 0.3 GPa and 750°C. This low pressure overlaps with the lower bound of M1, fitting the overall decompressive path followed by northern Sardinia migmatites (Giacomini et al., 2006, 2008). Thus, the PT conditions recorded by diatexite are considered representative of the M2 melting stage.

9.3 | P–T–t evolution

The Punta Bianca massif preserves clear field evidence of two distinct episodes of anatexis, as testified by the development of fractures and pseudotachylyte-bearing faults between the two melting stages. The M1 melting stage (Figure 13a) involves dehydration melting in the sillimanite stability field and is tentatively interpreted as related to the onset of regional anatexis in the early Carboniferous (360–340 Ma; Ferrara et al., 1978; Giacomini et al., 2006, 2008; Cruciani et al., 2016; Li et al., 2014). A few early Carboniferous zircon and monazite ages (340 Ma) retained by the orthogneiss provide a poorly constrained age for M1, which is however consistent with the ages obtained in the adjacent sites of NE Sardinia and southern Corsica (Ferrara et al., 1978; Giacomini et al., 2006, 2008; Li et al., 2014). Nevertheless, the PT paths of northern Sardinia and Punta Bianca migmatites become obviously divergent after M1, between about 337 and 310 Ma. The development of fractures and pseudotachylyte-bearing faults indicates substantial post-M1 cooling below the solidus, at temperatures not exceeding 600°C as indicated by brittle behaviour of feldspar (Hirth & Tullis, 1992; Rybacki & Dresen, 2000). This was followed by re-heating to above the solidus, culminating in the M2 melting stage (Figure 13a,b). The amount of M2 heating cannot be precisely quantified as the lowest temperature reached by the rocks before M2 is poorly constrained. Regardless of these uncertainties, the geochronological constraints indicate that M2 involved a substantial increase of temperature of up to 60–80°C after the development of pseudotachylytes (Points B to C in Figure 13a). All rocks shared a post-M2 retrograde evolution characterized by nearly isobaric cooling in the cordierite stability field ($P = 0.3$–0.25 GPa; Figure 13a).

It should be emphasized that the development of pseudotachylytes at sub-solidus conditions implies that the PT path of diatexite cannot result from nearly isothermal decompression after M1 but requires significant re-heating after exhumation to very low pressure < 0.3 GPa, in the cordierite stability field. Given the general decompressive path followed by the Variscan crust of N Sardinia, it seems likely that re-heating followed a nearly

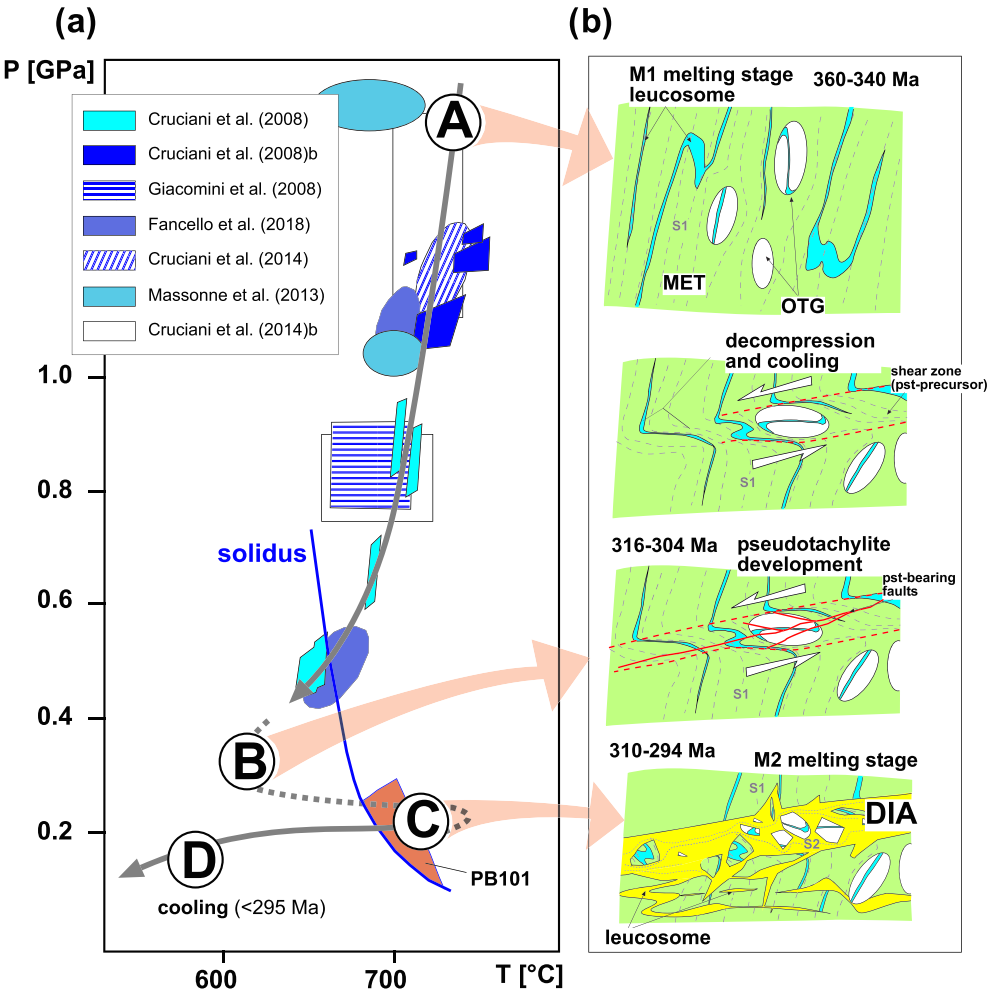

FIGURE 13 Evolution of the Punta Bianca massif: (a) reconstructed P–T–t-d path (grey line) compared with the regional dataset of thermo-barometric constraints from N Sardinia and southern Corsica, point A corresponds to the peak of M1 melting stage, point B represents the presumed conditions during pseudotachylyte development, point C marks the M2 melting stage (this study), point D corresponds to final cooling after M2; solidus curve after sample PB 101; (b) conceptual model showing the structural evolution of the Punta Bianca massif during decompression after M1 [Colour figure can be viewed at wileyonlinelibrary.com]

isobaric path. This interpretation is further confirmed by geochronological constraints, as the zircon age of diatexite indicates that the system crossed the solidus on cooling approximately at about 308 Ma (point C in Figure 13a).

9.4 | Origin of diatexite

9.4.1 | Heat sources for M2

The high melt proportion of diatexite requires that the rate of melt accumulation exceeded the rate at which melt escaped from the rock (White et al., 2005). Fast accumulation might be due to either addition of external melts (Greenfield et al., 1996), extremely efficient melt redistribution, at least at the outcrop-scale (e.g. Milord et al., 2001; Sawyer, 1998), or enhanced melt production (e.g. Hasalova et al., 2008). The first model can be ruled out, as the diatexite composition and REE patterns are broadly consistent with those of the other migmatite types in the study area. It should be emphasized that the composition of diatexite samples with the highest melt proportions, such as PB101a, is almost indistinguishable from that of orthogneiss, except a slight depletion of HREE (Figure 6a) that can be explained by fractionation of garnet during partial melting (e.g. Jung & Hellebrand, 2006). Another argument supporting the absence of exotic components is the widespread occurrence of Ordovician and early Palaeozoic zircon ages within diatexite, with age populations matching those of the metatexites. Based on these observations, we suggest that diatexite does not incorporate any externally sourced melt but rather formed from in situ melting of variable proportions of both types of metatexites.

The extreme variability of the relative proportion between protholith fragments and M2 melt in diatexite might reflect either different melt volumes produced due to spatially variable H_2O content, different melt redistribution rates or a combination thereof (Buick et al., 2004; Milord et al., 2001; White et al., 2005). The distinction between both processes is somewhat speculative, as the high degree of melting precludes tracing the melt pathways accurately. Yet, there is widespread evidence for

rotation, shearing and interactions between clasts of metatexites during magmatic flow (Figure 2); thus, it is reasonable that the variable structure of diatexite results from outcrop-scale melt migration rather than different melt production rates (Figure 13b). Regardless of the effectiveness of melt redistribution during M2, the P–T–t-d path captured by diatexite implies HTLP metamorphism and anatexis in the uppermost part of the continental crust, a condition which is rarely documented in convergent settings (i.e. Chopin et al., 2020).

This extreme metamorphic event apparently represents an exception in the Variscan crust of the Corsica–Sardinia block, as the age of anatexis is generally constrained as Lower Carboniferous (Ferrara et al., 1978; Giacomini et al., 2006, 2008). Yet the age of M2 is mostly coincident with the age of the precursors to peraluminous calc-alkaline plutons forming the Corsica–Sardinia Batholith (U2 plutons in Casini et al., 2012, 2015a,b; Rossi & Cocherie, 1991; Paquette et al., 2003). Thus, we argue that the study area represents a frozen magmatic source zone that escaped further melting and homogenization because of rapid exhumation of the crust, cooling, or both. Whatever the reason that led to preservation of pre-batholitic structures at Punta Bianca, isobaric reheating by up to 60–80°C and melting at low pressure requires an efficient heat source located in the uppermost crust. The detailed analysis of thermal sources driving this HTLP anatectic event is beyond the scope of this work, yet a few general remarks can be drawn by combining field structural observations, geochronology and petrological constraints.

First, magmatic underplating can be ruled out, as the only evidence for significant addition of mantle-derived melts are represented by Permian intrusions dated at least 20–30 Ma younger than M2 (Casini et al., 2012; Casini, Cuccuru, Maino, et al., 2015a; Renna et al., 2006, 2007). Moreover, the granitic plutons close to the Punta Bianca massif reveal systematically younger U–Pb ages than diatexite, indicating that M2 was not driven by contact metamorphism due to emplacement of either lower crustal or mantle-derived melts (Casini et al., 2015a,b). Alternative hypotheses include localized viscous shear heating, likely combined with fluid-fluxed melting or upwelling of hot asthenosphere. Both processes could potentially raise the crustal temperature by up to 100–150°C, although heating due to thermal input from the asthenospheric mantle would produce regional rather than local effects (Von Blanckenburg & Davies, 1995; Gerya et al., 2004). In this case, the M2 melting stage recorded by Punta Bianca migmatites could represent a rarely preserved regional event.

On the other hand, deformation processes might localize transient but significant thermal perturbations in narrow mylonitic/cataclastic shear zones. Long-term frictional-viscous deformation, in fact, accounts for moderate heating that results into localized thermal anomalies up to 150°C (Burg & Gerya, 2005; Casini et al., 2021; Casini & Maino, 2018; Maino et al., 2015, 2020). However, due to the difficulty to trace the shear heating signature and fluid pathways in high-grade rocks, further investigations are required to test the applicability of this mechanism.

9.4.2 | Evidence of fluid-fluxed melting

The large volume of melt formed in diatexite during the M2 melting stage cannot be explained by dehydration melting, because muscovite was already consumed during the M1 melting stage and the peak M2 temperature (Figure 7a) was insufficient to trigger biotite dehydration melting at 0.3–0.4 GPa (Breton & Thompson, 1988; Whitney, 1988). Thus, it is likely that the increased melt production recorded by diatexite during M2 involved refertilization of otherwise nearly anhydrous, refractory, lithotypes leading to fluid-fluxed melting (Holtz et al., 2001). The composition of diatexite supports this interpretation, as indicated by the occurrence of magmatic garnet (Alonso Perez et al., 2009) and the decrease of K_2O content relative to metatexite (Castro, 2013; Patiño Douce & Harris, 1998). Moreover, the lower Rb/Sr ratio of diatexite relative to metatexites (0.32–0.36 and 0.70–0.77, respectively) indicates that M2 melting reactions consumed dry assemblages containing plagioclase + quartz rather than hydrous phases (Weinberg & Hasalova, 2015). Finally, diatexites with relatively low melt content are characterized by M2 leucosomes with diffuse boundaries, as commonly observed in migmatites derived from fluid-fluxed melting of granitic orthogneiss (Weinberg & Hasalova, 2015).

Despite the recent reappraisal of fluid-fluxed melting as a viable mechanism to explain the production of large volumes of granitic magmas (i.e. Castro, 2020; Collins et al., 2016; Tafur & Diener, 2020), the general applicability of this mechanism is still largely debated, mainly because (i) the ductile crust has a low porosity and cannot host significant volumes of free water (Yardley, 2009) and (ii) the lower T water-saturated solidus prevents fluids from migrating to supra-solidus domains (Schorn et al., 2018). Yet the pseudotachylyte-bearing fault network indisputably reflects a seismic event with a significant dilatational component (Frohlich, 1995). Seismic deformation leads to nearly instantaneous increase of dynamic porosity due to co-seismic fracturing, establishing a pressure gradient that could have attracted external fluids within the damage zone, as proposed in other

ductile crustal sections characterized by strong rheological heterogeneities (e.g. Corvò et al., 2021; Jamtveit et al., 2018; Menegon et al., 2017).

Assuming that the mean volume of pseudotachylytes observed in the metatexitic orthogneiss (about 5–15 vol.%) represents an upper bound for transient porosity, we speculate that a corresponding volume of fluids might have been pumped into the shear zone, triggering M2 fluid-fluxed melting.

10 | CONCLUSIONS

The results of this study provide insights on the timing, conditions and processes of two-stage regional anatexis during exhumation of the Variscan orogenic root. Field structural analysis combined with pseudosection modelling and U–Pb LA-ICP-MS monazite dating indicates that the second anatectic event involved extensive melting under *HTLP* upper crustal conditions during the Carboniferous, resulting in the development of garnet-bearing diatexite. Crustal melting related to the development of diatexite implies a substantial re-heating of the Variscan crust following decompression and cooling after a first (early Carboniferous) melting stage. The contribution to the thermal budget of exotic melts is negligible. Re-heating and in situ melting of the upper crust is interpreted as generated by either a rarely preserved regional input of asthenospheric mantle or a local shear heating effect. The results of this work highlight the importance of combining field structural constraints, U–Pb geochronology and thermodynamic modelling for reconstructing the P–T–t-d path of high-grade terrains.

ACKNOWLEDGEMENTS

We wish to thank S. Schorn and one anonymous referee for providing careful and constructive reviews. The editors J. Diener and R. White are also greatly acknowledged for their supportive criticism and for helping us to improve the clarity of the paper. L. Casini thanks Regione Autonoma della Sardegna for partly supporting this research (grant no. RASSR14473) and Università di Sassari (FAR2020). J. Reche acknowledges support from the Spanish Ministerio de Economía, Industria y Competi-tividad through Projects: PID2019-109018RB-I00 and 2015-66335-C2-2-R. Open Access Funding provided by Universita degli Studi di Sassari within the CRUI-CARE Agreement.

ORCID

Leonardo Casini https://orcid.org/0000-0002-6157-1865
Matteo Maino https://orcid.org/0000-0001-8766-8027
Stefania Corvò https://orcid.org/0000-0003-2290-3967

REFERENCES

Albarède, F., & Michard-Vitrac, A. (1978). Age and significance of the North Pyrenean metamorphism. *Earth and Planetary Science Letters*, *40*, 327–332. https://doi.org/10.1016/0012-821X(78)90157-7

Alonso Perez, R., Müntener, O., & Ulmer, P. (2009). Igneous garnet and amphibolite fractionation in the roots of island arcs: Experimental constraints on andesite liquids. *Mineralogy and Petrology*, *157*, 541–558. https://doi.org/10.1007/s00410-008-0351-8

Breton, N. L., & Thompson, A. B. (1988). Fluid-absent (dehydration) melting of biotite in metapelites in the early stages of crustal anatexis. *Contributions to Mineralogy and Petrology*, *99*(2), 226–237. https://doi.org/10.1007/BF00371463

Buick, I. S., Stevens, G., & Gibson, R. L. (2004). The role of water retention in the anatexis of metapelites in the bushveld complex aureole, South Africa: An experimental study. *Journal of Petrology*, *45*, 1777–1797. https://doi.org/10.1093/petrology/egh033

Burg, J. P., & Gerya, T. V. (2005). The role of viscous heating in Barrovian metamorphism of collisional orogens: Thermomechanical models and application to the Lepontine dome in the Central Alps. *Journal of Metamorphic Geology*, *23*, 75–95. https://doi.org/10.1111/j.1525-1314.2005.00563.x

Burton, K. W., & O'Nions, R. K. (1992). The timing of mineral growth across a regional metamorphic sequence. *Nature*, *357*, 235–238. https://doi.org/10.1038/357235a0

Capitani, C., & Petrakakis, K. (2010). The computation of equilibrium assemblage diagrams with Theriak/domino software. *American Mineralogist*, *95*, 1006–1016. https://doi.org/10.2138/am.2010.3354

Carmignani, L., Carosi, R., Di Pisa, A., Gattiglio, M., Musumeci, G., Oggiano, G., & Pertusati, P. C. (1994). The Hercynian chain in Sardinia (Italy). *Geodinamica Acta*, *7*, 31–47. https://doi.org/10.1080/09853111.1994.11105257

Carosi, R., Montomoli, C., Tiepolo, M., & Frassi, C. (2012). Geochronological constraints on post-collisional shear zones in the Variscides of Sardinia (Italy). *Terra Nova*, *24*, 42–51. https://doi.org/10.1111/j.1365-3121.2011.01035.x

Casini, L. (2012). A MATLAB-derived software (geothermMOD1.2) for one-dimensional thermal modeling, and its application to the Corsica-Sardinia batholith. *Computers & Geosciences*, *45*, 82–86. https://doi.org/10.1016/j.cageo.2011.10.020

Casini, L., & Maino, M. (2018). 2D-thermo-mechanical modelling of spatial PT variations in heterogeneous shear zones, Italian. *Journal of Geosciences*, *137*(2), 272–282. https://doi.org/10.3301/IJG.2018.13

Casini, L., Cuccuru, S., Maino, M., Oggiano, G., Puccini, A., & Rossi, P. (2015a). Structural map of Variscan northern Sardinia (Italy). *Journal of Maps*, *11*, 1–10. https://doi.org/10.1080/17445647.2014.936914

Casini, L., Cuccuru, S., Maino, M., Oggiano, G., & Tiepolo, M. (2012). Emplacement of the Arzachena pluton (Corsica–Sardinia batholith) and the geodynamics of incoming Pangaea. *Tectonophysics*, *544-545*, 31–49. https://doi.org/10.1016/j.tecto.2012.03.028

Casini, L., & Funedda, A. (2014). Potential of pressure solution for strain localization in the Baccu Locci shear zone (Sardinia, Italy). *Journal of Structural Geology*, *66*, 188–204. https://doi.org/10.1016/j.jsg.2014.05.016

Casini, L., Cuccuru, S., Puccini, A., Oggiano, G., & Rossi, P. (2015b). Evolution of the Corsica–Sardinia Batholith and late-orogenic shearing of the Variscides. *Tectonophysics*, *646*, 65–78. https://doi.org/10.1016/j.tecto.2015.01.017

Casini, L., Maino, M., Sanfilippo, A., Ildefonse, B., & Dick, H. J. B. (2021). High-temperature strain localization and the nucleation of oceanic Core complexes (16.5° N, mid-Atlantic ridge). *Journal of Geophysical Research B: Solid Earth*, *126*, e2021JB022215.

Castro, A. (2013). Tonalite–granodiorite suites as cotectic systems: A review of experimental studies with applications to granitoid petrogenesis. *Earth-Science Reviews*, *124*, 68–95. https://doi.org/10.1016/j.earscirev.2013.05.006

Castro, A. (2020). The dual origin of I-type granites: The contribution of from experiments. *Geological Society of London, Special Pubblication*, *491*, 101–145. https://doi.org/10.1144/SP491-2018-110

Catlos, E. J., Gilley, L. D., & Harrison, T. M. (2002). Interpretation of monazite ages obtained via in situ analysis. *Chemical Geology*, *188*, 193–215. https://doi.org/10.1016/S0009-2541(02)00099-2

Cherniak, D. J., & Pyle, J. M. (2008). Th diffusion in monazite. *Chemical Geology*, *256*, 52–61. https://doi.org/10.1016/j.chemgeo.2008.07.024

Chopin, F., Korja, A., Nikkilä, K., Hölttä, P., Korja, T., Zaher, M. A., Kurhila, M., Eklund, O., & Rämö, O. T. (2020). The Vaasa Migmatitic complex (Svecofennian Orogen, Finland): Buildup of a LP-HT dome during Nuna assembly. *Tectonics*, *39*, e2019TC005583.

Cocco, F., Oggiano, G., Funedda, A., Casini, L., & Loi, A. (2018). Stratigraphic, magmatic and structural features of Ordovician tectonics in Sardinia (Italy): A review. *Journal of Iberian Geology*, *44*, 619–639. https://doi.org/10.1007/s41513-018-0075-1

Corfu, F., Hanchar, J. M., Hoskin, P. W. O., & Kinny, P. (2003). Atlas of zircon textures. In J. M. Hanchar & W. O. Hoskin (Eds.), *Zircon: Mineralogical Society of America, Reviews in Mineralogy and Geochemistry* (Vol. 53, pp. 468–500). Mineralogical Society of America.

Collins, W. J., Huang, H. Q., & Jiang, X. (2016). Water-fluxed crustal melting produces cordilleran batholiths. *Geology*, *44*, 143–146. https://doi.org/10.1130/G37398.1

Corvò, S., Maino, M., Langone, A., Schenker, F. L., Piazolo, S., Casini, L., & Seno, S. (2021). Local variations of metamorphic record from compositionally heterogeneous rocks (Cima di Gagnone, Central Alps): Inferences on exhumation processes of (U)HP-HT rocks. *Lithos*, *390-391*, 106126. https://doi.org/10.1016/j.lithos.2021.106126

Cruciani, G., Franceschelli, M., Caredda, A. M., & Carcangiu, G. (2001). Anatexis in the Hercynian basement of NE Sardinia, Italy: A case study of the migmatite of Porto Ottiolu. *Mineralogy and Petrology*, *71*(3), 195–233. https://doi.org/10.1007/s007100170039

Cruciani, G., Franceschelli, M., Elter, F. M., Puxeddu, M., & Utzeri, D. (2008a). Petrogenesis of Al–silicate-bearing trondhjemitic migmatites from NE Sardinia, Italy. *Lithos*, *102*, 554–574. https://doi.org/10.1016/j.lithos.2007.07.023

Cruciani, G., Franceschelli, M., Jung, S., Puxeddu, M., & Utzeri, D. (2008b). Amphibole-bearing migmatites from the Variscan Belt of NE Sardinia, Italy: Partial melting of mid-Ordovician igneous sources. *Lithos*, *105*, 208–224. https://doi.org/10.1016/j.lithos.2008.03.009

Cruciani, G., Franceschelli, M., Langone, A., & Puxeddu, M. (2019). U-Pb zircon and Ar-Ar amphibole ages from Sardinian migmatites (Italy) and review of migmatite ages from the Variscan belt. *Periodico di Mineralogia*, *88*, 203–219.

Cruciani, G., Franceschelli, M., Massonne, H. J., Musumeci, G., & Spano, M. E. (2016). Thermomechanical evolution of the high-grade core in the nappe zone of Variscan Sardinia, Italy: The role of shear deformation and granite emplacement. *Journal of Metamorphic Geology*, *34*, 321–342. https://doi.org/10.1111/jmg.12183

Cuccuru, S., Casini, L., Oggiano, G., & Cherchi, G. P. (2012). Can weathering improve the toughness of a fractured rock? A case study using the san Giacomo granite. *Bulletin of Engineering Geology and Environment*, *71*, 557–567. https://doi.org/10.1007/s10064-012-0416-9

Davies, J. H., & Von Blanckenburg, F. (1995). Slab breakoff: A model of lithosphere detachment and its test in the magmatism and deformation of collisional orogens. *Earth and Planetary Science Letters*, *129*, 85–102.

De Vraies van Leeuwen, A. T., Hand, M., Morrissey, L. J., & Raimondo, T. (2021). Th-U powered metamorphism: Thermal consequences of a chemical hotspot. *Journal of Metamorphic Geology*, *39*, 541–565.

Deer, W. A., Howie, R. A., & Zussman, J. (1966). *An introduction to the rock-forming minerals* (p. 528). Longman Group Limited.

Del Moro, A., Di Simplicio, P., Ghezzo, C., Guasparri, G., Rita, F., & Sabatini, G. (1975). Radiometric data and intrusive sequence in the Sardinian batholith. *Neues Jahrbuch Für Mineralogie*, (Abhandlungen) 126, 28–44.

Depine, G. V., Andronicos, C. L., & Phipps-Morgan, J. (2008). Near-isothermal conditions in the middle and lower crust induced by melt migration. *Nature*, *452*, 80–83. https://doi.org/10.1038/nature06689

Diener, J. F. A., & Powell, R. (2010). Influence of ferric iron on the stability of mineral assemblages. *Journal of Metamorphic Geology*, *28*, 599–613. https://doi.org/10.1111/j.1525-1314.2010.00880.x

Ducoux, M., Jolivet, L., Callot, J.-P., Aubourg, C., Masini, E., Lahfid, A., Homonnay, E., Cagnard, F., Gumiaux, C., & Baudin, T. (2019). The nappe des Marbres unit of the Basque-Cantabrian Basin: The Tectono-thermal evolution of a fossil hyperextended Rift Basin. *Tectonics*, *38*, 3881–3915. https://doi.org/10.1029/2018TC005348

Edel, J. B., Casini, L., Oggiano, G., Rossi, P., & Schulmann, K. (2014). Early Permian 90° clockwise rotation of the Maures-Estérel- Corsica-Sardinia block confirmed by new palaeomagnetic data and followed by a Triassic 60° clockwise rotation. *Geological Society Special Publication*, *405*, 1–29.

Erickson, T. M., Pearce, M. A., Taylor, R. J. M., Timms, N. E., Clark, C., Reddy, S. M., & Buick, I. S. (2015). Deformed monazite yields high-temperature tectonic ages. *Geology*, *43*, 383–386. https://doi.org/10.1130/G36533.1

Evensen, N. M., Hamilton, P. J., & O'nions, R. K. (1978). Rare-earth abundances in chondritic meteorites. *Geochimica et Cosmochimica Acta*, *42*, 1199–1212. https://doi.org/10.1016/0016-7037(78)90114-X

Fancello, D., Cruciani, G., Franceschelli, M., & Massonne, H. J. (2018). Trondhjemitic leucosomes in paragneisses from NE Sardinia: Geochemistry and P-T conditions of melting and crystallization. *Lithos*, *304-307*, 501–517. https://doi.org/10.1016/j.lithos.2018.02.023

Faye, G. H. (1968). The optical absorption spectra of certain transition metal ions in muscovite, lepidolite and fuchsite. *Canadian Journal of Earth Science*, *5*, 31–38. https://doi.org/10.1139/e68-003

Ferrara, G., Ricci, C. A., & Rita, F. (1978). Isotopic ages and tectono-metamorphic history of the metamorphic basement of north-eastern Sardinia. *Contributions to Mineralogy and Petrology*, *68*, 99–106. https://doi.org/10.1007/BF00375451

Forbes, W. C., & Flower, M. F. J. (1974). Phase relations of titan-phlogopite, K2Mg4TiAl2Si6O20(OH)4: A refractory phase in the upper mantle? *Earth Planetary Science Letters*, *22*, 60–66. https://doi.org/10.1016/0012-821X(74)90064-8

Frohlich, C. (1995). Characteristics of well determined non-double-couple earthquakes in the Harvard CMT catalogue. *Physics of the Earth and Planetary Interiors*, *91*, 213–228. https://doi.org/10.1016/0031-9201(95)03031-Q

Gasquet, D., Bertrand, J.-M., Paquette, J.-L., Lehmann, J., Ratzov, G., De Ascencao Guedes, R., Tiepolo, M., Boullier, A. M., & Scaillet, S. (2010). Miocene to Messinian deformation and hydrothermal activity in a pre-Alpine basement massif of the French western Alps: New U-Th-Pb and argon ages from the Lauzière massif. *Bulletin de la Société Géologique de France*, *181*, 227–241. https://doi.org/10.2113/gssgfbull.181.3.227

Gébelin, A., Roger, F., & Brunel, M. (2009). Syntectonic crustal melting and high-grade metamorphism in a transpressional regime, Variscan massif central, France. *Tectonophysics*, *477*, 229–243. https://doi.org/10.1016/j.tecto.2009.03.022

Gerdes, A., Wörner, G., & Henk, A. (2000). Post-collisional granite generation and HT-LP metamorphism by radiogenic heating: The Variscan south bohemian batholith. *Journal of the Geological Society*, *157*, 577–587. https://doi.org/10.1144/jgs.157.3.577

Gerya, T. V., Yuen, D. A., & Maresch, W. V. (2004). Thermomechanical modelling of slab detachment. *Earth and Planetary Science Letters*, *226*, 101–116. https://doi.org/10.1016/j.epsl.2004.07.022

Giacomini, F., Bomparola, R. M., & Ghezzo, C. (2005). Petrology and geochronology of metabasites with eclogite facies relics from NE Sardinia: Constraints for the Palaeozoic evolution of southern Europe. *Lithos*, *82*, 221–248. https://doi.org/10.1016/j.lithos.2004.12.013

Giacomini, F., Bomparola, R. M., Ghezzo, C., & Guldbransen, H. (2006). The geodynamic evolution of the southern European Variscides: Constraints from the U/Pb geochronology and geochemistry of the lower Palaeozoic magmatic-sedimentary sequences of Sardinia (Italy). *Contributions to Mineralogy and Petrology*, *152*, 19–42. https://doi.org/10.1007/s00410-006-0092-5

Giacomini, F., Dallai, L., Carminati, E., Tiepolo, M., & Ghezzo, C. (2008). Exhumation of a Variscan orogenic complex: Insights into the composite granulitic–amphibolitic metamorphic basement of south-East Corsica (France). *Journal of Metamorphic Geology*, *26*, 403–436. https://doi.org/10.1111/j.1525-1314.2008.00768.x

Gibson, H. D., Carr, S. C., Brown, R. L., & Hamilton, M. A. (2004). Correlations between chemical and age domains in monazite, and metamorphic reactions involving major pelitic phases: an integration of ID-TIMS and SHRIMP geochronology with Y–Th–U X-ray mapping. *Chemical Geology*, *211*, 237–260. https://doi.org/10.1016/j.chemgeo.2004.06.028

Grand'Homme, A., Janots, E., Seydoux-Guillaume, A.-M., Guillaume, D., Bosse, V., & Magnin, V. (2016). Partial resetting of the U-Th-Pb systems in experimentally altered monazite: Nanoscale evidence of incomplete replacement. *Geology*, *44*, 4–7. https://doi.org/10.1130/G37770.1

Green, E. C. R., Holland, T. J. B., Powell, R., & White, R. W. (2012). Garnet and spinel lherzolite assemblages in MgO-Al2O3-SiO2 and CaO-MgO-Al2O3-SiO2: Thermodynamic models and an experimental conflict. *Journal of Metamorphic Geology*, *30*, 561–577. https://doi.org/10.1111/j.1525-1314.2012.00981.x

Greenfield, J. E., Clarke, G. L., Bland, M., & Clark, D. C. (1996). In-situ migmatite and hybrid diatexite at Mt Stafford, Central Australia. *Journal of Metamorphic Geology*, *14*, 363–378. https://doi.org/10.1046/j.1525-1314.1996.06002.x

Guernina, S., & Sawyer, E. W. (2003). Large-scale melt-depletion in granulite terranes: An example from the Archean Ashuanipi subprovince of Quebec. *Journal of Metamorphic Geology*, *21*, 181–201. https://doi.org/10.1046/j.1525-1314.2003.00436.x

Harlov, D. E., Wirth, R., & Hetherington, C. J. (2011). Fluid-mediated partial alteration in monazite: The role of coupled dissolution–reprecipitation in element redistribution and mass transfer. *Contributions to Mineralogy and Petrology*, *162*, 329–348. https://doi.org/10.1007/s00410-010-0599-7

Hasalova, P., Schulmann, K., Lexa, O., Štípská, P., Hrouda, F., Ulrich, S., Haloda, J., & Týcová, P. (2008). Origin of migmatites by deformation-enhanced melt infiltration of orthogneiss: A new model based on quantitative microstructural analysis. *Journal of Metamorphic Geology*, *26*, 29–53. https://doi.org/10.1111/j.1525-1314.2007.00743.x

Henry, D. J., & Guidotti, C. V. (2002). Titanium in biotite from metapelitic rocks: Temperature effects, crystal-chemical controls, and petrologic applications. *American Mineralogist*, *87*, 375–382. https://doi.org/10.2138/am-2002-0401

Hiess, J., Condon, D. J., McLean, N., & Noble, S. R. (2012). 238U/235U systematics in terrestrial uranium-bearing minerals. *Science*, *335*, 1610–1614. https://doi.org/10.1126/science.1215507

Hirth, G., & Tullis, J. (1992). Dislocation creep regimes in quartz aggregates. *Journal of Structural Geology*, *14*, 145–159. https://doi.org/10.1016/0191-8141(92)90053-Y

Holland, T. J. B., & Powell, R. (2003). Activity-composition relations for phases in petrological calculations: An asymmetric multicomponent formulation. *Contributions to Mineralogy and Petrology*, *145*, 492–501. https://doi.org/10.1007/s00410-003-0464-z

Holland, T. J. B., & Powell, R. (2011). An improved and extended internally consistent thermodynamic dataset for phases of petrological interest, involving a new equation of state for solids. *Journal of Metamorphic Geology*, *29*, 333–383. https://doi.org/10.1111/j.1525-1314.2010.00923.x

Holtz, F., Johannes, W., Tamic, N., & Behrens, H. (2001). Maximum and minimum water contents of granitic melts: Implications for chemical and physical properties of ascending magmas. *Lithos*, *56*, 1–14. https://doi.org/10.1016/S0024-4937(00)00056-6

Horstwood, S. A., Foster, G. L., Parrish, R. R., Noble, S. R., & Nowell, G. M. (2003). Common-Pb corrected in situ U–Pb accessory mineral geochronology by LA–MC–ICP–MS. *Journal of Analytical Atomic Spectrometry.*, *18*, 837–846. https://doi.org/10.1039/B304365G

Hoskin, P. W. O. (2005). Trace-element composition of hydrothermal zircon and the alteration of hadean zircon from the Jack Hills, Australia. *Geochimica et Cosmochimica Acta*, *69*, 637–648. https://doi.org/10.1016/j.gca.2004.07.006

Jackson, S. E., Pearson, N. J., Griffin, W. L., & Belousova, E. A. (2004). The application of laser ablation-inductively coupled plasma-mass spectrometry to in situ U-Pb zircon geochronology. *Chemical Geology*, *211*, 47–69. https://doi.org/10.1016/j.chemgeo.2004.06.017

Jamtveit, B., Ben-Zion, Y., Renard, F., & Austrheimn, H. (2018). Earthquake-induced transformations of the lower crust. *Nature*, *556*, 487–491. https://doi.org/10.1038/s41586-018-0045-y

Janots, E., Negro, F., Brunet, F., Goffé, B., Engi, M., & Bouybaouène, M. L. (2006). Evolution of the REE mineralogy in HP–LT metapelites of the Sebtide complex, Rif, Morocco: Monazite stability and geochronology. *Lithos*, *87*, 214–234. https://doi.org/10.1016/j.lithos.2005.06.008

Jaupart, C., & Marechal, J. C. (2007). Heat flow and thermal structure of the lithosphere: Treatise on. *Geophysics*, *6*, 217–251.

Johannes, W. (1984). Beginning of melting in the granite system Qz-or-ab-an-H_2O. *Contributions to Mineralogy and Petrology*, *86*, 264–273. https://doi.org/10.1007/BF00373672

Jung, S., & Hellebrand, E. (2006). Trace element fractionation during high-grade metamorphism and crustal melting—Constraints from ion microprobe data of metapelitic, migmatitic and igneous garnets and implications for Sm–Nd garnet chronology. *Lithos*, *87*, 193–213. https://doi.org/10.1016/j.lithos.2005.06.013

Ketchum, J. W. F., Jackson, S. E., Culshaw, N. G., & Barr, S. M. (2001). Depositional and tectonic setting of the Palaeoproterozoic lower Aillik group, Makkovik Province, Canada: Evolution of a passive margin–foredeep sequence based on petrochemistry and U– Pb (TIMS and LAM-ICP-MS) geochronology. *Precambrian Research*, *105*, 331–356. https://doi.org/10.1016/S0301-9268(00)00118-2

Kohn, M. J. (2016). Metamorphic chronology—A tool for all ages: Past achievements and future prospects. *American Mineralogist*, *101*(1), 25–42. https://doi.org/10.2138/am-2016-5146

Kohn, M. J., Wieland, M. S., Parkinson, C. D., & Upreti, B. N. (2005). Five generations of monazite in Langtang gneisses: Implications for chronology of the Himalayan metamorphic core. *Journal of Metamorphic Geology*, *23*, 399–406. https://doi.org/10.1111/j.1525-1314.2005.00584.x

Kumar, P. S., Menon, R., & Reddy, G. K. (2007). The role of radiogenic heat production in the thermal evolution of a Proterozoic granulite-facies orogenic belt: Eastern Ghats, Indian shield. *Earth and Planetary Science Letters*, *254*, 39–54. https://doi.org/10.1016/j.epsl.2006.11.018

Langone, A., José, P.-N., & A., Ji, W. Q., Zanetti, A., Mazzucchelli, M., Tiepolo, M., Giovanardi, T., Bonazzi, M. (2017). Ductile–brittle deformation effects on crystal-chemistry and U–Pb ages of magmatic and metasomatic zircons from a dyke of the Finero Mafic Complex (Ivrea–Verbano Zone, Italian Alps). *Lithos*, *284-285*, 493–511. https://doi.org/10.1016/j.lithos.2017.04.020

Langone, A., Braga, R., Massonne, H. J., & Tiepolo, M. (2011). Preservation of old (prograde metamorphic) U–Th–Pb ages in unshielded monazite from the high-pressure paragneisses of the Variscan Ulten Zone (Italy). *Lithos*, *127*(1–2), 68–85. https://doi.org/10.1016/j.lithos.2011.08.007

Langone, A., Zanetti, A., Daczko, N. R., Piazolo, S., Tiepolo, M., & Mazzucchelli, M. (2018). Zircon U-Pb dating of a lower crustal shear zone: A case study from the northern sector of the Ivrea-Verbano zone (Val Cannobina, Italy). *Tectonics*, *37*, 322–342. https://doi.org/10.1002/2017TC004638

Lexa, O., Schulmann, K., Janoušek, V., Štípská, P., Guy, A., & Racek, M. (2011). Heat sources and trigger mechanisms of exhumation of HP granulites in Variscan orogenic root. *Journal of Metamorphic Geology*, *29*, 79–102. https://doi.org/10.1111/j.1525-1314.2010.00906.x

Li, X. H., Faure, M., Lin, W. 2014. From crustal anatexis to mantle melting in the Variscan orogen of Corsica (France): SIMS U-Pb zircon age constraints. Tectonophysics, 634, 19-30. ff10.1016/j.tecto.2014.07.021f.

Locock, A. J. (2008). An excel spreadsheet to recast analyses of garnet into end-member components, and a synopsis of the crystal chemistry of natural silicate garnets. *Computers & Geosciences*, *34*, 1769–1780. https://doi.org/10.1016/j.cageo.2007.12.013

Ludwig, K.R. 2003. Isoplot/Ex Version 3.0: a Geochronological Toolkit for Microsoft Excel, 4 Berkeley Geochronology Center, Special Publication (2003), p. 70

Maino, M., Dallagiovanna, G., Gaggero, L., Seno, S., & Tiepolo, M. (2012). U–Pb zircon geochronological and petrographic constraints on late to post-collisional Variscan magmatism and metamorphism in the Ligurian Alps, Italy. *Geological Journal*, *47*, 632–652. https://doi.org/10.1002/gj.2421

Maino, M., Casini, L., Ceriani, A., Decarlis, A., Di Giulio, A., Seno, S., Setti, M., & Stuart, F. M. (2015). Dating shallow thrusts with zircon (U-Th)/he thermochronometry—The shear heating connection. *Geology*, *43*(6), 495–498. https://doi.org/10.1130/G36492.1

Maino, M., Gaggero, L., Langone, A., Seno, S., & Fanning, M. (2019). Cambro-Silurian magmatisms at the northern Gondwana margin (Penninic basement of the Ligurian Alps). *Geoscience Frontiers*, *10*, 315–330. https://doi.org/10.1016/j.gsf.2018.01.003

Maino, M., Casini, L., Boschi, C., Setti, M., Di Giulio, A., & Seno, S. (2020). Time-dependent heat budget of a thrust from geological records and numerical experiments. *Journal of Geophysical Research, Solid Earth*, *125*(3), e2019JB018940. https://doi.org/10.1029/2019JB018940

Marotta, A. M., & Spalla, M. I. (2007). Permian-Triassic high thermal regime in the Alps: Result of late Variscan collapse or continental rifting? Validation by numerical modeling. *Tectonics*, *26*(4), TC4016.

Martínez Catalán, J. R. (2012). The central Iberian arc, an orocline centered in the Iberian Massif and some implications for the Variscan belt. *International Journal of Earth Sciences*, *101*, 1299–1314. https://doi.org/10.1007/s00531-011-0715-6

Martins, L., Farias, S. R., Valdecir, V., & Janasi de, A. (2009). Reaction microtextures of monazite: Correlation between chemical and age domains in the Nazaré Paulista migmatite, SE Brazil. *Chemical Geology*, *261*, 271–285. https://doi.org/10.1016/j.chemgeo.2008.09.020

Massonne, H. J., Franceschelli, M., & Cruciani, G. (2013). Geothermobarometry on anatectic melts – A high pressure Variscan migmatite from Northeast Sardinia. *International Geology Review*, *55*, 1490–1505. https://doi.org/10.1080/00206814.2013.780720

Matte, P. (2001). The Variscan collage and orogeny (480-290 ma) and the tectonic definition of the Armorica microplate: A review. *Terra Nova*, *13*, 122–128. https://doi.org/10.1046/j.1365-3121.2001.00327.x

Menegon, L., Pennacchioni, G., Malaspina, N., Harris, K., & Wood, E. (2017). Earthquakes as precursors of ductile shear zones in the dry and strong lower crust. *Geochemistry, Geophysics, Geosystems*, *18*, 4356–4374. https://doi.org/10.1002/2017GC007189

Milan, L. A., Daczko, N. R., Clarke, G. L., & Allibone, A. H. (2016). Complexity of In-situ zircon U–Pb–Hf isotope systematics during arc magma genesis at the roots of a Cretaceous arc, Fiordland, New Zealand. *Lithos*, *264*, 296–314. https://doi.org/10.1016/j.lithos.2016.08.023

Milord, I., Sawyer, E. W., & Brown, M. (2001). Formation of diatexite migmatite and granite magma during anatexis of semi-pelitic metasedimentary rocks: An example from St. Malo. *France. Journal of Petrology*, *42*, 487–505. https://doi.org/10.1093/petrology/42.3.487

Nabelek, P. I., & Liu, M. (1999). Leucogranites in the Black Hills of South Dakota: The consequence of shear heating during continental collision. *Geology*, *27*, 523–526. https://doi.org/10.1130/0091-7613(1999)027<0523:LITBHO>2.3.CO;2

Nabelek, P. I., Liu, M., & Sirbescu, M. L. (2001). Thermo-rheological, shear heating model for leucogranite generation, metamorphism, and deformation during the Proterozoic trans-Hudson orogeny, Black Hills. *South Dakota. Tectonophysics*, *342*(3), 371–388. https://doi.org/10.1016/S0040-1951(01)00171-8

Nabelek, P. I., Whittington, A. G., & Hofmeister, A. M. (2010). Strain heating as a mechanism for partial melting and ultrahigh temperature metamorphism in convergent orogens: Implications of temperature-dependent thermal diffusivity and rheology. *Journal of Geophysical Research: Solid Earth*, *115*, 1–18. https://doi.org/10.1029/2010JB007727

Oggiano, G., Gaggero, L., Funedda, A., Buzzi, L., & Tiepolo, M. (2010). Multiple early Paleozoic volcanic events at the northern Gondwana margin: U-Pb age evidence from the southern Variscan branch (Sardinia, Italy). *Gondwana Research*, *17*(1), 44–58. https://doi.org/10.1016/j.gr.2009.06.001

Padovano, M., Dörr, W., Elter, F. M., & Gerdes, A. (2014). The East Variscan Shear Zone: Geochronological constraints from the Capo Ferro area (NE Sardinia, Italy). *Lithos*, *196-197*, 27–41. https://doi.org/10.1016/j.lithos.2014.01.015

Paquette, J.-L., Ménot, R.-P., Pin, C., & Orsini, J.-B. (2003). Episodic and short-lived granitic pulses in a post-collisional setting: Evidence from precise U-Pb zircon dating through a crustal cross-section in Corsica. *Chemical Geology*, *198*, 1–20. https://doi.org/10.1016/S0009-2541(02)00401-1

Paquette, J.-L., & Tiepolo, M. (2007). High resolution (5 μm) U-Th-Pb isotope dating of monazite with excimer laser ablation (ELA)-ICPMS. *Chemical Geology*, *240*, 222–237. https://doi.org/10.1016/j.chemgeo.2007.02.014

Paterson, B. A., Stephens, W. E., Williams, I. S., Hinton, R. W., & Herd, D. A. (1992). The nature of zircon inheritance in two granite plutons. In P. E. Brown & B. W. Chappel (Eds.), *In 'The second hutton symposium on the origin of granites and related rocks'*. GSA Special Papers. https://doi.org/10.1130/SPE272-p459

Patiño Douce, A. E., & Harris, N. (1998). Experimental constraints on Himalayan anatexis. *Journal of Petrology*, *39*(4), 689–710. https://doi.org/10.1093/petroj/39.4.689

Piazolo, S., Austrheim, H., & Whitehouse, M. (2012). Brittle-ductile microfabrics in naturally deformed zircon: Deformation mechanisms and consequences for U-Pb dating. *American Mineralogist*, *97*, 1544–1563. https://doi.org/10.2138/am.2012.3966

Piazolo, S., La Fontaine, A., Trimby, P., Harley, S., Yang, L., Armstrong, R., & Cairney, J. M. (2016). Deformation-induced trace element redistribution in zircon revealed using atom probe tomography. *Nature Communications*, *7*(1), 1–7. https://doi.org/10.1038/ncomms10490

Platt, J. P. (2015). Influence of shear heating on microstructurally defined plate boundary shear zones, Journal of Structural Geology, 79, 80–89, https://doi.org/10.1016/j.jsg.2015.07.009

Pownall, J. M. (2015). UHT metamorphism on Seram, eastern Indonesia: Reaction microstructures and P–T evolution of spinel-bearing garnet–sillimanite granulites from the Kobipoto Complex. *Journal of Metamorphic Geology*, *33*, 909–935. https://doi.org/10.1111/jmg.12153

Pyle, J. M., & Spear, F. S. (2003). Four generations of accessory-phase growth in low-pressure migmatites from SW New Hampshire. *American Mineralogist*, *88*, 338–351. https://doi.org/10.2138/am-2003-2-311

Powell, R., White, R. W., Green, E. C. R., Holland, T. J. B., & Diener, J. F. A. (2014). On parameterising thermodynamic descriptions of minerals for petrological calculations. *Journal of Metamorphic Geology*, *32*, 245–260. https://doi.org/10.1111/jmg.12070

Rebay, G., Powell, R., & Diener, J. F. A. (2010). Calculated phase equilibria for a MORB composition in a *P–T* range, 450–650°C and 18–28 kbar: The stability of eclogite. *Journal of Metamorphic Geology*, *28*, 635–645. https://doi.org/10.1111/j.1525-1314.2010.00882.x

Renna, M. R., Tribuzio, R., & Tiepolo, M. (2006). Interaction between basic and acid magmas during the latest stages of the post-collisional Variscan evolution: Clues from the gabbro–granite association of Ota (Corsica–Sardinia batholith). *Lithos*, *90*, 92–110. https://doi.org/10.1016/j.lithos.2006.02.003

Renna, M. R., Tribuzio, R., & Tiepolo, M. (2007). Origin and timing of the post-Variscan gabbro–granite complex of Porto (Western Corsica). *Contributions to Mineralogy and Petrology*, *154*, 493–517. https://doi.org/10.1007/s00410-007-0205-9

Robert, J.-L. (1976). Titanium solubility in synthetic phlogopite solid solutions. *Chemical Geology*, *17*, 213–227. https://doi.org/10.1016/0009-2541(76)90036-X

Rolin, P., Marquer, D., Colchen, M., Cartannaz, C., Cocherie, A., Thiery, V., Quenardel, J.-M., & Rossi, P. (2009). Famenno-carboniferous (370-320 ma) strike slip tectonics monitored by syn-kinematic plutons in the French Variscan belt (massif Armoricain and French massif central). *Bulletin de la Societé Geologique de France*, *180*, 231–246. https://doi.org/10.2113/gssgfbull.180.3.231

Rossi, P., & Cocherie, A. (1991). Genesis of a Variscan batholith: Field, petrological and mineralogical evidence from the Corsica-Sardinia batholith. *Tectonophysics*, *195*(2–4), 319–346. https://doi.org/10.1016/0040-1951(91)90219-I

Rubatto, D. (2002). Zircon trace element geochemistry: Distribution coefficients and the link between U-Pb ages and metamorphism. *Chemical Geology*, *184*, 123–138. https://doi.org/10.1016/S0009-2541(01)00355-2

Rudnick, R. L., & Gao, S. (2003). Composition of the Continental Crust, vol 3. In H. D. Holland & K. K. Turekian (Eds.), *Treatise on geochemistry: Meteorites, comets and planets* (Vol. 1) (pp. 59–659). Elsevier Ltd.. https://doi.org/10.1016/B0-08-043751-6/03016-4

Rybacki, E., & Dresen, G. (2000). Dislocation and diffusion creep of synthetic anorthite aggregates. *Journal of Geophysical Research*, *105*(B11), 26017–26036. https://doi.org/10.1029/2000JB900223

Sandiford, M., & McLaren, S. (2002). Tectonic feedback and the ordering of heat producing elements within the continental lithosphere. *Earth and Planetary Science Letters*, *204*, 133–150. https://doi.org/10.1016/S0012-821X(02)00958-5

Savko, K. A., Samsonov, A. V., & Sal'nikova, E. B., Kotov, A. B., Bazikov, N. S. (2015). HT/LP metamorphic zoning in the eastern Voronezh crystalline massif: Age and parameters of metamorphism and its geodynamic environment. *Petrology*, *23*, 559–575. https://doi.org/10.1134/S0869591115050045

Sawyer, E. W. (1998). Formation and evolution of granite magmas during crustal reworking: The significance of diatexites. *Journal of Petrology*, *39*, 1147–1167. https://doi.org/10.1093/petroj/39.6.1147

Sawyer, E. W. (1999). Criteria for the recognition of partial melting. *Physics and Chemistry of the Earth, Part A: Solid Earth and Geodesy*, *24*, 269–279. https://doi.org/10.1016/S1464-1895(99)00029-0

Sawyer, E. W. (2020). Petrogenesis of secondary diatexite and the melt budget for crustal reworking. *Journal of Petrology*, *61*(3), egaa039. https://doi.org/10.1093/petrology/egaa039

Schorn, S., Diener, J. F. A., Powell, R., & Stuwe, K. (2018). Thermal buffering in the orogenic crust. *Geology*, *46*, 643–646. https://doi.org/10.1130/G40246.1

Secchi, F., Casini, L., Cifelli, F., Naitza, S., Carta, E., & Oggiano, G. (2022). Syntectonic magmatism and reactivation of collisional structures during late-Variscan shearing (SW Sardinia, Italy). *International Journal of Earth Sciences*, *111*, 1469–1490. https://doi.org/10.1007/s00531-022-02193-2

Seydoux-Guillaume, A.-M., Paquette, J.-L., Wiedenbeck, M., Montel, J. M., & Heinrich, W. (2002). Experimental resetting of the U–Th–Pb systems in monazite. *Chemical Geology*, *191*, 165–181. https://doi.org/10.1016/S0009-2541(02)00155-9

Smye, A. J., Greenwood, L. V., & Holland, T. J. B. (2010). Garnet-chloritoid-kyanite assemblages: Eclogite facies indicators of subduction constraints in orogenic belts. *Journal of Metamorphic Geology*, *28*, 753–768. https://doi.org/10.1111/j.1525-1314.2010.00889.x

Spear, F. S., & Pyle, J. M. (2002). Apatite, monazite and xenotime in metamorphic rocks. *Reviews in Mineralogy and Geochemistry*, *48*, 293–335. https://doi.org/10.2138/rmg.2002.48.7

Spear, F. S., & Pyle, J. M. (2010). Theoretical modeling of monazite growth in a low-ca pelite. *Chemical Geology*, *273*, 111–119. https://doi.org/10.1016/j.chemgeo.2010.02.016

Spencer, C. J., Cavosie, A. J., Raub, T. D., Rollinson, H., Jeon, H., Searle, M. P., Miller, J. A., & EIMF, McDonald, B.J. Evans, N. J. (2017). Evidence for melting mud in Earth's mantle from extreme oxygen isotope signatures in zircon. *Geology*, *45*, 975–978. https://doi.org/10.1130/G39402.1

Stepanov, A. S., Hermann, J., Rubatto, D., & Rapp, R. P. (2012). Experimental study of monazite/melt partitioning with implications for the REE, Th and U geochemistry of crustal rocks. *Chemical Geology*, *300-301*, 200–220. https://doi.org/10.1016/j.chemgeo.2012.01.007

Tafur, L. A., & Diener, J. F. A. (2020). Mineral equilibrium constraints on the feasibility of diffusive H2O-fluxed melting in the continental crust. *Journal of Metamorphic Geology*, *38*, 719–742. https://doi.org/10.1111/jmg.12536

Tiepolo, M. (2003). In situ Pb geochronology of zircon with laser ablation inductively coupled plasma-sector field mass spectrometry. *Chemical Geology*, *192*, 1–19. https://doi.org/10.1016/S0009-2541(03)00083-4

Timms, N. E., Erickson, T. M., Pearce, M. A., Cavosie, A. J., Schmieder, M., Steven, E. T., Reddy, M., Zanetti, M. R., Nemchin, A. A., & Wittmann, A. (2017). A pressure-temperature phase diagram for zircon at extreme conditions. *Earth Sciences Review*, *165*, 185–202. https://doi.org/10.1016/j.earscirev.2016.12.008

van Achterberg, E., Ryan, C. G., Jackson, S. E., & Griffin, W. (2001). Data reduction software for LA–ICP–MS. In P. Sylvester (Ed.), *Laser ablation ICPMS in the earth science: Principles and applications* (Vol. 29, pp. 239–243). Mineralogical Association of Canada.

White, R. W., Pomroy, N. E., & Powell, R. (2005). An in situ metatexite–diatexite transition in upper amphibolite facies rocks from Broken Hill, Australia. *Journal of Metamorphic Geology*, *23*, 579–602. https://doi.org/10.1111/j.1525-1314.2005.00597.x

White, R. W., Powell, R., Holland, T. J. B., & Worley, B. A. (2000). The effect of TiO2 and Fe2O3 on metapelitic assemblages at greenschist and amphibolite facies conditions: Mineral equilibria calculations in the system K2O-FeO-MgO-Al2O3-SiO2-H2O-TiO2-Fe2O3. *Journal of Metamorphic Geology*, *18*, 497–511. https://doi.org/10.1046/j.1525-1314.2000.00269.x

White, R., Powell, R., & Holland, T. J. B. (2001). Calculation of partial melting equilibria in the system Na2O-CaO-K2O-FeO-MgO-Al2O3-SiO2-H2O (NCKFMASH). *Journal of Metamorphic Geology*, *19*, 139–153. https://doi.org/10.1046/j.0263-4929.2000.00303.x

White, R. W., Powell, R., & Clarke, G. L. (2002). The interpretation of reaction textures in Fe-rich metapelitic granulites of the

Musgrave block, Central Australia: Constraints from mineral equilibria calculations in the system K2O-FeO-MgO-Al2O3--SiO2-H2O-TiO2-Fe2O3. *Journal of Metamorphic Geology*, *20*, 41–55. https://doi.org/10.1046/j.0263-4929.2001.00349.x

White, R. W., Powell, R., Holland, T. J. B., Johnson, T. E., & Green, E. C. R. (2014a). New mineral activity-composition relations for thermodynamic calculations in metapelitic systems. *Journal of Metamorphic Geology*, *32*, 261–286.

White, R. W., Powell, R., & Johnson, T. E. (2014b). The effect of Mn on mineral stability in metapelites revisited: New a-x relations for manganese-bearing minerals. *Journal of Metamorphic Geology*, *32*, 809–828. https://doi.org/10.1111/jmg.12095

Whitney, J. A. (1988). The origin of granite: The role and source of water in the evolution of granitic magmas. *Geological Society of America Bulletin*, *100*(12), 1886–1897. https://doi.org/10.1130/0016-7606(1988)100<1886:TOOGTR>2.3.CO;2

Wiedenbeck, M., Alle, P., Corfu, F., Griffin, W. L., Meier, M., Oberli, F., Vonquadt, A., Roddick, J. C., & Speigel, W. (1995). W. Three natural zircon standards for U-Th-Pb, Lu-Hf, trace element and REE analyses. *Geostandards Newsletter*, *19*, 1–23. https://doi.org/10.1111/j.1751-908X.1995.tb00147.x

Will, T. M. (1998). *Phase equilibria in metamorphic rocks: Thermodynamic background and petrological applications* (Vol. 71 (Lecture Notes in Earth Sciences)). Springer. ISBN-10: 3540641548

Williams, I. S. (1992). Some observations on the use of zircon U-Pb geochronology in the study of granitic rocks. Earth and Environmental Science Transactions of The Royal Society of Edinburgh. In *Second hutton symposium: The origin of granites and related rocks* (Vol. 83, Issue 1–2, pp. 447–458). Cambridge University Press.

Yardley, B. W. D. (2009). The role of water in the evolution of the continental crust. *Journal of the Geological Society, London*, *166*, 585–600. https://doi.org/10.1144/0016-76492008-101

Zhang, J.-R., Wei, C.-J., & Chu, H. (2018). High-T and low-P metamorphism in the Xilingol Complex of central Inner Mongolia, China: An indicator of extension in a previous orogeny. *Journal of Metamorphic Geology*, *36*, 393–417. https://doi.org/10.1111/jmg.12297

SUPPORTING INFORMATION

Additional supporting information can be found online in the Supporting Information section at the end of this article.

Table S1. Isotopic analyses of zircon grains from metatexitic orthogneiss, pseudotachylyte and diatexite.

Table S2. Isotopic analyses of monazite grains from diatexite.

How to cite this article: Casini, L., Maino, M., Langone, A., Oggiano, G., Corvò, S., Estrada, J. R., & Liesa, M. (2022). HTLP metamorphism and fluid-fluxed melting during multistage anatexis of continental crust (N Sardinia, Italy). *Journal of Metamorphic Geology*, 1–33. https://doi.org/10.1111/jmg.12687